Reconstruction of Electromagnetic Showers and Determination of the Position Resolution of a Prototype of the $\overline{\text{P}}$ANDA Electromagnetic Calorimeter

Diplomarbeit
im Fachgebiet Experimentalphysik
Prof. Dr. Volker Metag
II. Physikalisches Institut
Universität Gießen

vorgelegt von

Daniel Andreas Bremer
aus Lohra

Betreuer: Dr. Rainer Novotny

Contents

Summary **1**

1 Introduction **3**
1.1 Physics of PANDA and Importance of the Calorimeter 4
1.2 Properties of the Electromagnetic Shower 7
1.2.1 Shower Development and Natural Units 7
1.2.2 Shower Propagation 10
1.3 Demands on a Calorimeter: Energy, Position and Time Information . . 12

2 The Experiment: PROTO60 **17**
2.1 Technical Design of the Detector 17
2.1.1 Mechanical Design 17
2.1.2 Test Readout 19
2.2 Test Measurement Performance 22
2.3 Energy Calibration 24

3 Data Analysis **29**
3.1 Shower Energy Reconstruction 29
3.1.1 Line Shapes 29
3.1.2 Energy Response 30
3.2 Time Resolution 34
3.2.1 Difficulties 34
3.2.2 Linearisation 35
3.2.3 Achieved Resolutions 37
3.3 Position Reconstruction 41
3.3.1 Theoretical Considerations 41
3.3.2 Position Reconstruction 42
3.3.3 Influence of the Beamspot on the Reconstruction 45
3.3.4 Achieved Position Resolutions 48

4 Comparison to Simulations on the Basis of PandaROOT **51**
4.1 The PandaROOT Software Package 51
4.2 Assumptions 52

4.3 First Results 54
4.3.1 Energy Resolution 54
4.3.2 Position Resolution 55

5 Discussion and Outlook **61**
5.1 Achieved Results in Comparison to the TDR and General Expectations 61
5.2 Comparison to Simulations and Unsolved Issues 63
5.3 Improvement of Calibration Methods 65
5.3.1 Vertically Mounted PROTO60 65
5.3.2 Cross of Inorganic Fibers for Beam Monitoring 65

List of Figures **V**

List of Tables **IX**

Bibliography **XI**

Summary

The electromagnetic calorimeter of $\overline{\mathrm{P}}$ANDA is an essential device to achieve the ambitous physical goals, especially due to the expected high detection efficiency for photons and electrons. Beside a good energy resolution of this lead tungstate based device, it is necessary to have a sufficient position and time resolution. Therefore, detailed testing of prototypes is needed. In February 2009, a test run at the Mainz electron accelerator facility MAMI was performed with a prototype (PROTO60), which represents a subsection of the barrel detector and consists of a 6×10 matrix of tapered lead tungstate crystals. A tagged photon beam with energies from 0.150 GeV - 1.441 GeV impinged on the prototype at four different beam positions.

The analysis of this test run includes a reconstruction of the electromagnetic shower and the determination of the impact point of the incident photon. Different algorithms of position calculation were investigated. A simple center of gravity algorithm delivered narrow distributions but also systematic shifts. For a logarithmic weighting, taking into account the exponential falloff of the electromagnetic shower, smaller systematic shift was observed. With this algorithm, the calculated position was nearly independent of the energy of the incoming photon, while the position resolution showed the expected energy dependence. This is true for both cartesian coordinates, x and y. The determination of the intrinsic resolution was not possible due to the uncertainty of the beam shape. Therefore an upper limit for the position resolution of 4.3 mm at 1 GeV was achieved, if all crystals of the detector were taken into account for the reconstruction. But also for reduced subunits of the prototype, namely a 5×5 and a 3×3 matrix, position calculations were performed.

Investigations of time information were performed and a non-linearity in the energy dependence was observed and corrected. The walk effect was fitted with a 4-parameter function, which afterwards was subtracted from the original time spectra. This procedure provided a time resolution of the PROTO60 central detector of 680 ps at 1 GeV, while the resolution averaged over the whole energy range amounts to 1.2 ns.

Simulations with the detector specific PandaROOT framework, based on the Monte-Carlo transport model Geant4, were performed. The simulation results, taking into account only the deposited energy information and no dead material between the crystals as well as the impact on light collection, photon statistics or electronics, agree well with the experimental results concerning position reconstruction. The deduced

energy resolution indicates the limits for an ideal detector. Nevertheless the shower shape, characterised by ratios of deposited energy in different detector subarrays, seems to be reproduced very well.

Chapter 1

Introduction

The $\overline{\mathrm{P}}$ANDA[1] experiment will be placed at the future facility FAIR[2] at the GSI[3] (Darmstadt, Germany; see Fig. 1.1). It is designed to perform strong interaction

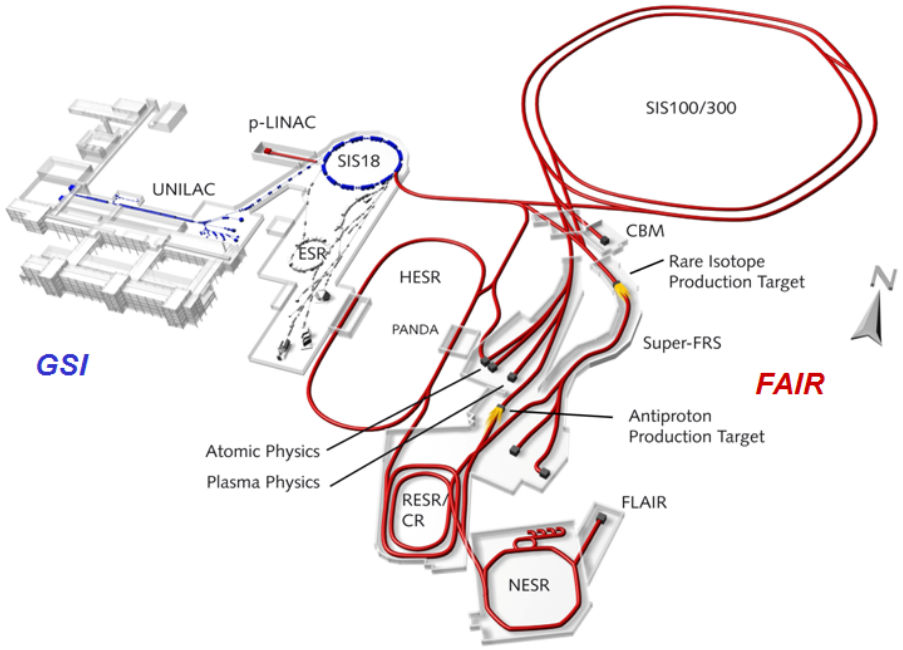

Figure 1.1: Artistic view of the present GSI (blue) and the planned future facility FAIR (red). The $\overline{\mathrm{P}}$ANDA Detector is located in the center of one straight sector of the HESR.

studies by observing reactions originating from the annihilation of antiprotons, stored and accelerated in the HESR[4], on nuclear targets, e.g. pellets of frozen hydrogen. The

[1] Anti**P**roton **AN**nihilations at **DA**rmstadt
[2] **F**acility for **A**ntiproton and **I**on **R**esearch
[3] **G**esellschaft für **S**chwer**I**onenforschung
[4] Abbreviation of **H**igh **E**nergy **S**torage **R**ing

resolution and geometrical quality of the antiproton beam with momenta between 1.5 GeV/c to 15 GeV/c is achieved by usage of both, stochastical and electron cooling reaching a maximum luminosity of $2 \cdot 10^{32} \frac{1}{\mathrm{cm^2 s}}$. This will allow a very accurate control of the beam energy, which is crucial to measure the masses of resonances and hadrons with a precision of 50 keV to 100 keV, which is roughly one or two orders of magnitude better compared to corresponding experiments at electron-positron-colliders. In addition, the antiproton-annihilation approach allows to form states with quantum numbers J^{PC}, that are not limited to the quantum numbers available in exclusively electroweak interactions.

1.1 Physics of PANDA and Importance of the Calorimeter

One characteristic feature of the strong interaction and its corresponding fundamental theory, the Quantum-Chromo-Dynamics (henceforth called QCD), is the strong dependence of the interaction strength, expressed in the quantity of the coupling constant α_S, on the distance over which the interaction occurs. The QCD is well understood at short distances and high Center of Mass (C-M-S) Energies where quantitative calculations with perturbation theory are possible due to the weakness of the interaction ($\alpha_S << 1$). The understanding at larger distance is rather crude. In this non-perturbative region the interaction is strong ($\alpha_S \approx 1$) and calculations are difficult, but also the experimental knowledge is limited.

At $\overline{\mathrm{P}}$ANDA, antiprotons and the fixed internal target will collide at C-M-S energies between 2.2 GeV/c and 5.5 GeV/c, surrounded by a detector designed for general purpose. The non-perturbative regime is fully accessable, as shown in Fig. 1.2. There is a widespread spectrum of physical topics adressed at $\overline{\mathrm{P}}$ANDA. Just a few of these will be explained in greater detail here:

Charmonium Spectroscopy The non-perturbative QCD gives a lot of predictions for the structure of the different excited Charmonium states (Quark Content: $c\bar{c}$). One prediction computed in Lattice-QCD is illustrated in Fig. 1.3. From the experimental point of view, an accurate measurement of existing states is very important for a deeper understanding of the theory. The possibility to populate all charmonium states without quantum number limitation will allow the investigation of states in significant numbers which otherwise would only be populated by secondary reactions. Furthermore this has the advantage, that the resolution will be mainly dominated by the beam quality.

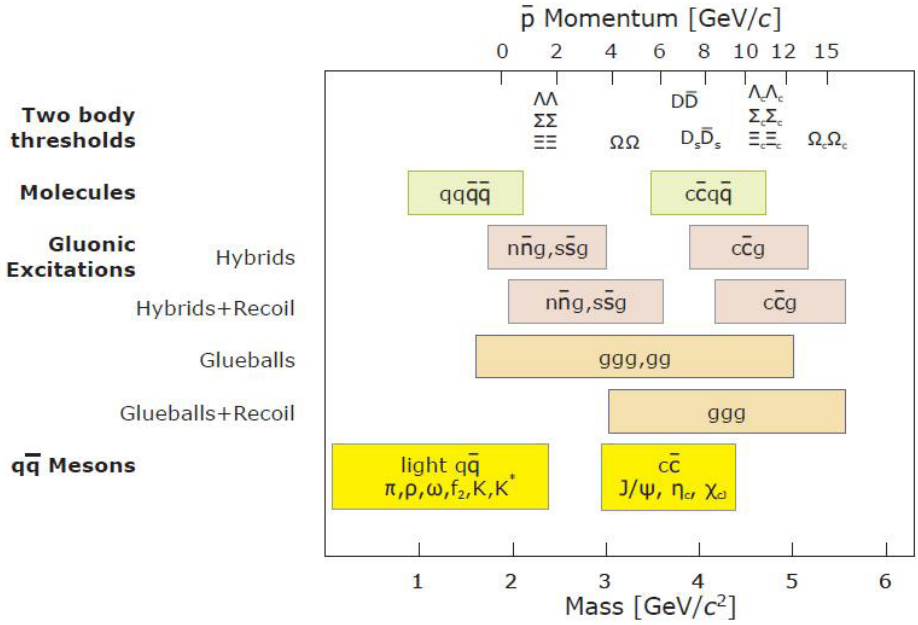

Figure 1.2: Accessible mass range (abscissa below) with respect to the required antiproton momentum (abscissa above).

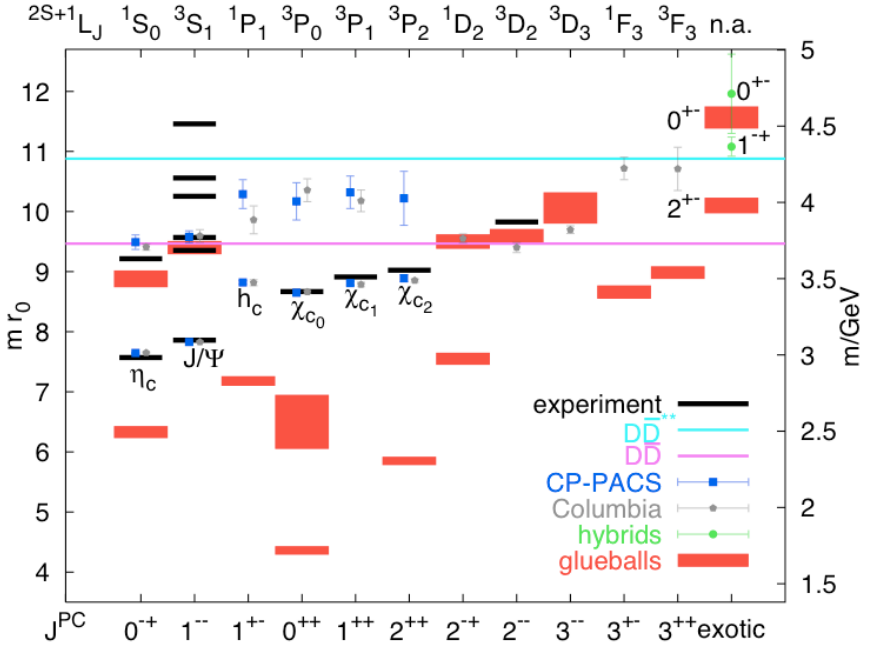

Figure 1.3: Lattice-QCD predictions for the charmonium, the glueball and the spin-exotic $c\bar{c}$-glue hybrids spectrum in quenched lattice QCD.

Search for Gluonic Excitations The existence of gluonic excitations is a fundamental feature of QCD. In general, there are two groups of gluonic excitations: On the one hand states consisting only of gluons, so called glueballs and on the other hand hybrid states consisting of quarks and gluons, both carrying degrees of freedom. For this reason gluonic excitations should be able to carry exotic quantum numbers J^{PC} forbidden for pure quark-antiquark states. Additionaly, glueballs should decay flavour blind, because they contain no valence quarks. Previous investigations concerning glueballs, especially in the low energy sector, showed ambiguous results. For example one candidate state, the $f_0(1500)$, measured by CrystalBarrel@LEAR[5], carries the quantum numbers 0^{++}, which is non-exotic. Indeed there is one state left in the corresponding scalar nonett, but $f_0(1500)$ shows a strong mixing of the glueball states with light meson states, resulting in a non-flavour-blind decay. As shown in Fig. 1.3, predictions favor the energy region from 3 - 5 GeV with a few states and most of them do not overlap with the charmonium states. Furthermore there are states which carry exotic quantum numbers and hence should be more easily identified by $\overline{\text{P}}$ANDA.

Study of Hadrons in Nuclear Matter Experiments which study in-medium modifications of hadrons to reach a better understanding concerning the origin of hadron masses have so far been restricted to light quarks. Now $\overline{\text{P}}$ANDA provides the opportunity to extend these studies towards the charmed quark sector. Other studies focus on the cross section for charmonium or D-meson production in different nuclear environments.

Open Charm Spectroscopy Next to the charmonium spectroscopy it will be possible to study the properties of a large number of charmed mesons, even beyond the $D\bar{D}$-Threshold.

Hypernuclear Physics If one replaces an up- or down-quark with a heavier strange-quark, one will get a so called hypernucleus. In fact, the usual nuclear chart gets an additional degree of freedom, resulting in a three- dimensional nuclear chart as shown in Fig. 1.4.

Electromagnetic Processes Another approach to study the nucleon structure is the investigation of electromagnetic processes. Via the reaction $\bar{p}p \rightarrow e^+e^-$ $\overline{\text{P}}$ANDA will be able to measure the electromagnetic form factor of the proton over a large range of the momentum transfer q^2. Also other electromagnetic processes, like wide angle Compton scattering will be accessible.

[5] **L**ow **E**nergy **A**ntiproton **R**ing

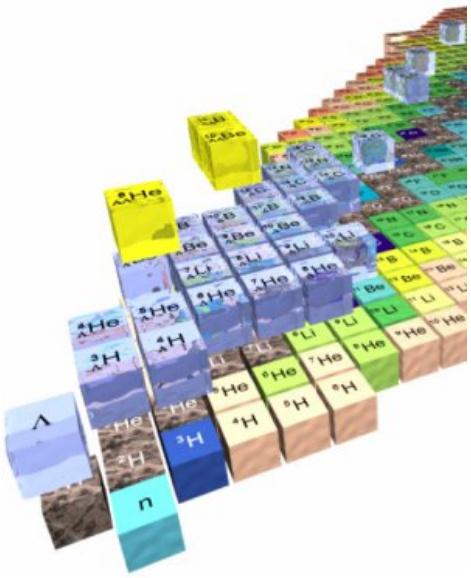

Figure 1.4: Artists view of the Hypernuclear Chart.

As seen above, most of the physical aims rely on a good performance of the $\overline{\text{P}}$ANDA detector, especially on its ability to measure the energy of produced secondary particles with a high precision over an extremely wide energy range. The only device which can measure the energy directly and can detect photons with high efficiency over 99 % of the solid angle is the electromagnetic calorimeter. An observation of a hybrid via decay channels, as shown in Fig. 1.5, is only possible by detecting all of the up to eight photons in the final state. Thus, a precise and robust calorimeter is absolutely necessary. The electromagnetic calorimeter of $\overline{\text{P}}$ANDA is therefore one of the main components to assure the achievement of the ambitious physics program.

1.2 Properties of the Electromagnetic Shower

1.2.1 Shower Development and Natural Units

The first electromagnetic showers, induced by high energy cosmic rays, were observed in 1933. With the development of medium and high energy particle accelerators, the reconstruction of electromagnetic showers became a common task in calorimetry. An EM shower is in principle a cascade of photons, electrons and positrons. As shown in Fig. 1.6 an incoming photon hitting the absorber or detector material has three options to interact with matter: photo effect, Compton effect and electron positron pair production or conversion. Since the cross section of the latter process rises with

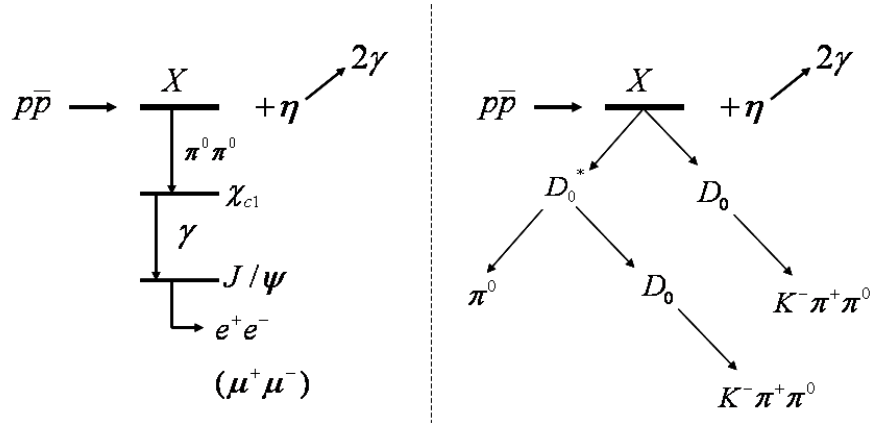

Figure 1.5: Two possible decays of a hybrid state called X. Each π^0 decays in two photons. Altogether one ends up with 7 photons in the final state for the left reaction or 8 photons for right reaction, respectively.

photon energy, Pair Production becomes the dominating mechanism at energies above a few MeV. Thus a high energetic photon produces in an absorber material with high atomic number Z electrons and positrons with a large probability. Those particles

Kind of Interaction	**Cross Section Dependence**
Photo Effect	$\propto \frac{Z^{4-5}}{E^{\frac{7}{2}}}$
Compton Effect	$\propto \frac{Z}{E}$
Pair Production	
...low energy, no screening	$\propto Z^2 \ln E$
...low energy, screening	$\propto Z^2 \ln \frac{1}{\sqrt[3]{Z}}$

Table 1.1: Cross section dependence on energy and atomic number for different interactions of photons with matter.

usually interact with the surrounding matter by ionisation processes, or if the energy exceeds the critical Energy E_c given by

$$E_c = \frac{550\text{MeV}}{Z} \tag{1.1}$$

in this material, by emission of bremsstrahlung. In fact, bremsstrahlung produces photons, which again can produce electrons/positrons due to conversion in secondary interactions. The development of the electromagnetic shower ends, as soon as the energy of the secondary particles is not sufficient anymore for conversion or the energy of the leptons is reduced below the critical energy. The threshold equates to $E =$

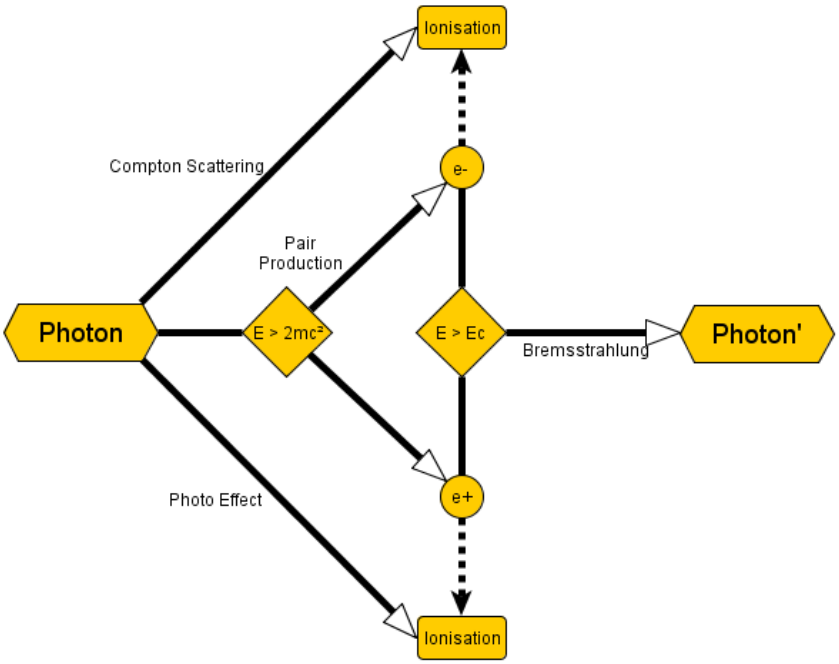

Figure 1.6: Schematic view of the development of an electromagnetic shower

$2m_e c^2$, where m_e is the electron/positron mass and c the velocity of light in vacuum. Since the stopping power $-\frac{dE}{dx}$ of electrons with kinetic energy E larger than E_c due to bremsstrahlung is much higher than the stopping power due to ionisation, the energy loss can be described by

$$-\frac{dE}{dx} = \frac{E}{X_0} \tag{1.2}$$

with the Radiation length X_0. Equation 1.2 can be solved by

$$E = E_0 e^{-\frac{x}{X_0}}. \tag{1.3}$$

X_0 is the mean pass length, after which the energy of an electron E is only $\frac{1}{e}$ of its incident energy E_0. It can be directly calculated for different materials with atomic mass A by using

$$X_0 = \frac{716.4 \cdot A}{Z(Z+1)\ln(\frac{287}{\sqrt{Z}})} \left[\frac{g}{cm^2}\right] \tag{1.4}$$

although in practice usually the following approximation is used:

$$X_0 = 180 \frac{A}{Z^2} \left[\frac{g}{cm^2}\right]. \tag{1.5}$$

For high energy photons, if only conversion has to be taken into account, an analogue parameter, the interaction length Λ is defined.

$$\Lambda = \frac{1}{\sigma_{Pair} N} = \frac{9}{7} X_0 \tag{1.6}$$

Λ is the interaction length, after which the number of incoming photons has been reduced by a factor $\frac{1}{e}$. X_0 and Λ can be used as scaling factor to determine the absorber volume to contain the complete EM shower irrespectively of the material.

1.2.2 Shower Propagation

The propagation of an electromagnetic shower can be split in two components, the longitudinal shower distribution in direction of the incident particle and in the transversal or lateral direction. The longitudinal distribution of the shower determines how deep the shower penetrates into the absorber and depends on the energy E of the incident particle in a logarithmic manner. With the parameters $y = \frac{E}{E_C}$ (and $t = \frac{x}{X_0}$) one can calculate the depth of the highest energy deposition in the material t_{max} or the depth of the center of gravity of the shower t_{cg} for the different incident particles according to Tab. 1.2. As indicated, the sum of the track length of all charged particles T is for both cases the same and directly given by y. Experiment and theory differ slightly in

	Incident Photon	**Incident Electron**
t_{max}	$1.01 \times [\ln y - 0.5]$	$1.01 \times [\ln y - 1]$
t_{cg}	$t_{max} + 1.7$	$t_{max} + 1.4$
T	y	y

Table 1.2: Determination of the longitudinal distribution of an electromagnetic shower caused by photons or electrons [LR09]. All units are given in terms of X_0.

the absolute values of the constant terms. Both relations show clearly, that the depth of the shower scales with the logarithm of the incident energy

$$t_{max,cg} \propto \ln E \tag{1.7}$$

as can be seen in Fig. 1.7 for photons of different energies in thallium doped caesium iodide ($Cs(Tl)$). As an estimate, an electromagnetic cascade deposits approximately 98% of the incident energy in an absorber with $L \approx 3t_{cg}$ length (in terms of X_0). This is important for the design of a calorimeter with respect to the compactness. Shower leakages through the rear end of an absorber with insufficient thickness will limit strongly the energy resolution due to the fluctuations of the shower.

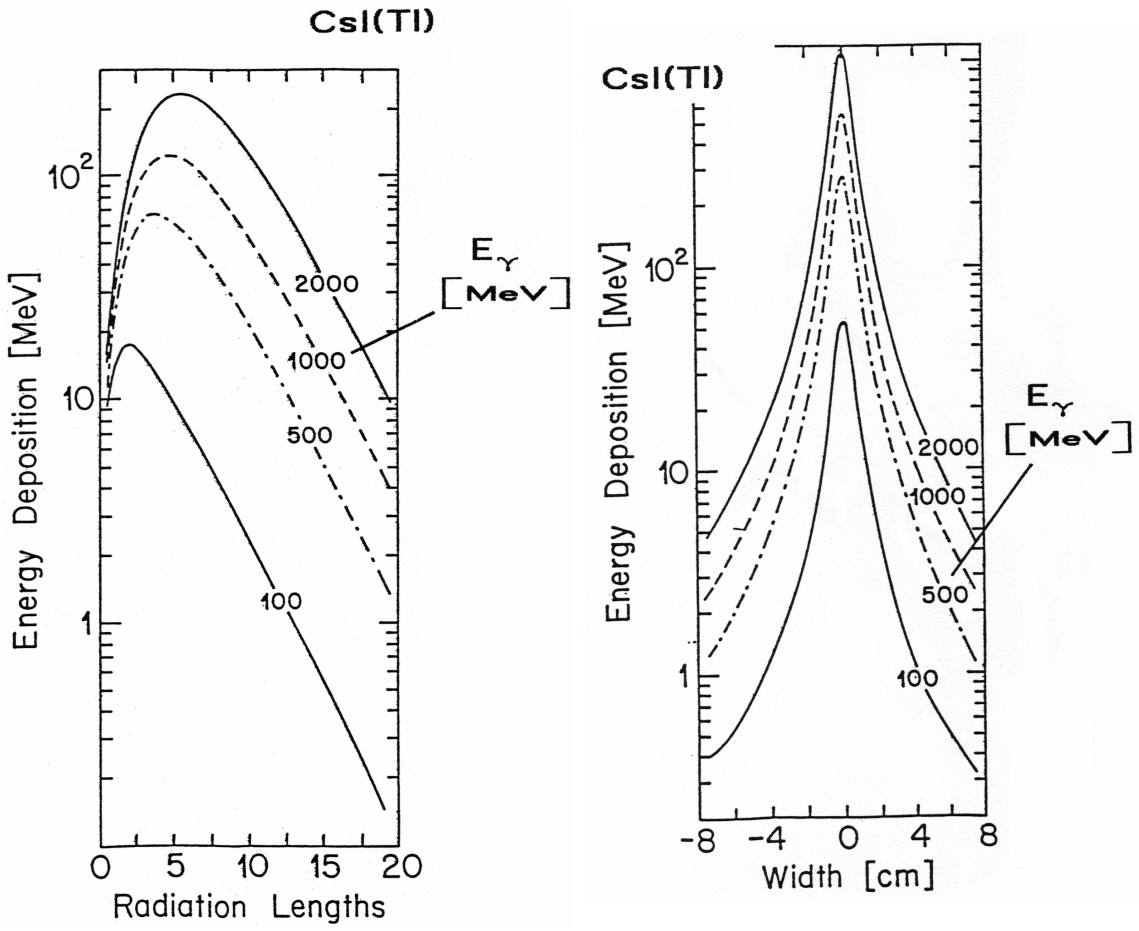

Figure 1.7: Longitudinal (left) and transversal (right) shower distribution in $CsI(Tl)$, which has a radiation length $X_0 = 1.85$ cm and Molière radius $R_M = 3.8$ cm [K$^+$85].

The lateral spread of the EM shower is mainly determined by multiple scattering of electrons and the angular distribution of bremsstrahlung. But also Compton scattering and the photoelectric effect produce particles, which are no longer aligned to the direction of the incoming particle. The mean lateral deflection of electrons of critical energy after passing through a thickness of X_0 is called the Molière Radius R_M and given by

$$R_M = \frac{21 \text{ MeV}}{E_C} X_0[\frac{\text{g}}{\text{cm}^3}] \approx \frac{7A}{Z\rho}[\text{cm}]. \tag{1.8}$$

A value of 95 % of the total energy is deposited in a cylinder centered around the incident track with radius $R = 2R_M$. A transverse shower profile is illustrated in Fig. 1.7. In calorimetry the detector is often laterally segmented. The point of impact of the incident particle can be deduced from the energy distribution in the responding elements. The width of one single unit often corresponds to $1R_M$ in order to make a compromise between energy and spatial resolution.

1.3 Demands on a Calorimeter: Energy, Position and Time Information

The performance of an electromagnetic calorimeter (EMC) is mainly determined by its ability to measure the energy of an incoming particle, the point of impact on the detector surface, and the minimum time needed to distinguish two consecutive signals.

How precise a homogeneous calorimeter based on scintillator material can measure the energy depends on the one hand on the fraction of the full shower energy deposited in the active volume and on the other hand on the response of the active material. For the former reason, an EM calorimeter composed completely of scintillator material, which serves as active absorber, is superior to a sampling calorimeter, which consists of alternating layers of absorber and active segments. The scintillation process is a statistical production of secondary particles and their quantity N is proportional to the deposited energy. Hence, according to Poisson statistics, the energy dependence of the relative energy resolution $\frac{\sigma_E}{E}$ scales according to

$$N \propto E \Rightarrow \frac{\sigma_E}{E} \propto \frac{1}{\sqrt{E}} \tag{1.9}$$

The value of the proportionality constant is governed by the amount of secondary particles per deposited energy unit, namely the light yield. Geometrical issues, like the amount of dead material and leakages caused by insufficient volume or relative

calibration are nearly independent on energy and therefore contribute to the energy resolution by a constant term. In addition, the noise of readout electronics can influence the achievable resolution at lower energies. This is often considered by an additional term in the parametrisation proportional to $\frac{1}{E}$. Altogether the relative energy resolution can be parametrized by the expression

$$\frac{\sigma_E}{E} = a \oplus \frac{b}{E} \oplus \frac{c}{\sqrt{E}} \tag{1.10}$$

If the detector is segmented laterally, position information on the point of impact of the incident particle can be deduced. The position is determined by weighting the position of the individual segments with the amount of energy deposited by the shower. The precision of this method is antiproportional to the size of the individual segments in terms of the Molière radius. However too small subdetectors will reduce the energy resolution due to the larger amount of dead material. Position determination is essential for the calculation of the invariant mass of primary particles like e.g. neutral pions, which decay into a pair of photons with a specific opening angle. The time resolution is mainly limited by the intrinsic decay kinetics of the scintillation material, but the readout electronics plays a significant role, too. The observation of high interaction rates or time of flight (TOF) measurements is only possible with a good time resolution.

The electromagnetic calorimeter of $\overline{\text{P}}$ANDA is designed for the special challenges brought up by the physics program described in section 1.1. The main requirements are as follow:

- Compactness
- Fast response to handle high interaction rates
- Sufficient energy resolution over a large energy range
- Radiation hardness to guarantee long operation periods

To satisfy this demands, lead tungstate ($PbWO_4$, also called PWO) was chosen. It has a short radiation length of $X_0 = 0.89$ cm and a Molière radius of $R_M = 2.1$ cm and thus allows a very compact design. Moreover, the short decay time of the gaussian distributed scintillation light with a mean wavelength of $\lambda = 420$nm of about 5 - 15 ns is sufficient for the expected high interaction rates. The $\overline{\text{P}}$ANDA EMC consists of two main parts, a target EMC, near the interaction vertex and a forward EMC placed downstream in beam direction. The target spectrometer, shown in Fig. 1.8, consists of three seperate parts, a barrel section, surrounding the beam pipe in a distance of roughly a half meter, and two endcaps, placed downstream and upstream of the target, called forward and backward endcap, respectively. The whole target EMC consists of approximately 16,000 PWO-II crystals with 23 different geometries that are cooled down to a temperature of $T = -25°$, which increases the light

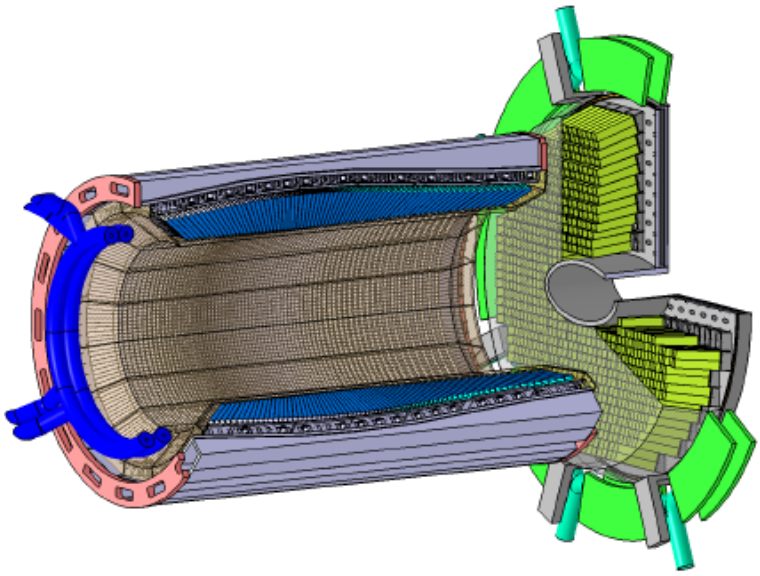

Figure 1.8: Schematic cross section of the target spectrometer. In this view, the backward endcap is missing

output further and therefore enhances the achievable energy resolution. Large-Area-Avalanche-Photodiodes (LAAPDs) serve as photosensors for the barrel EMC and the backward endcap, because the use of photomultipliers is not possible in the magnetic field of the solenoid. For the forward endcap a mix of LAAPDs and Vacuum-Photo-Triodes, which have a higher rate capability, is foreseen. The tapered crystals in each subdetector are shaped in a way, that they cover the same solid angle and the mean diameter of a crystal corresponds to approximately $1R_M$. This high granularity should be sufficient to deliver a good position resolution. Its impact on the invariant mass calculation of reconstructed pions is shown in Fig. 1.9. The figure also shows simulation results for the hit rate in the barrel EMC in dependence on the position. The high rate in the most forward crystals (high indices) indicates the importance of a good time resolution, also for the barrel detector. At these rates, that are even higher in the forward endcap, i.e. for the innermost crystals close to the beam beam pipe, a high radiation hardness is inevitable. This is achieved by optimized doping with rare earth ions and a sophisticated growing method. An overview over the required performance values for the different properties is given in Tab. 1.3. To ensure the quality and functionality of the future detector and to understand the behavior under different conditions, intensive prototyping is needed. Therefore a prototype of the barrel EMC was tested and the results will be presented in this thesis.

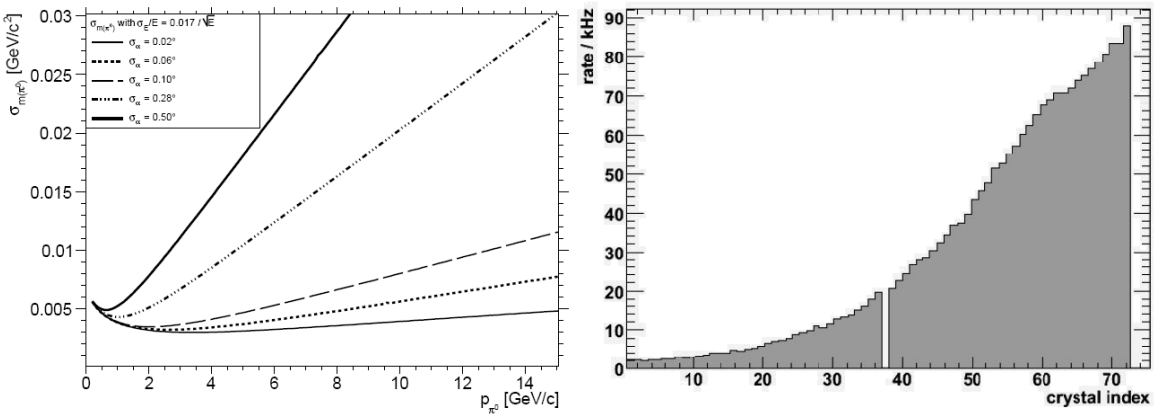

Figure 1.9: Dependence of the achievable invariant mass resolution $\sigma_{m(\pi^0)}$ of π^0 decaying into two γ on the momentum for different values of the spatial resolution σ_ϑ (left). Simulation result of the hit rate per detector in the barrel at an antiproton beam momentum of 14 GeV/c versus the crystal index (right). The gap corresponds to the opening for the pellet target.

Property	**Required Performance Value**
Energy resolution $\frac{\sigma_E}{E}$	$\leq 1\% \oplus \frac{\leq 2\%}{\sqrt{E}}$
Energy threshold E_{Thres}	10 MeV (20 MeV tolerable)
Energy threshold single crystal E_{xtl}	3 MeV
RMS noise (energy equivalent) $\sigma_{E,noise}$	1 MeV
Time Resolution for the relevant hit time t_0	≤ 3 ns
Barrel Specific Properties	
Energy range from E_{Thres}	7.3 GeV
Angular equivalent of crystal size ϑ	4°
Spatial Resolution σ_ϑ	0.3°
Radiation Hardness (max. annual dose)	10 Gy

Table 1.3: Several selected requirements for the $\overline{\text{P}}$ANDA EMC.

Chapter 2

The Experiment: PROTO60

2.1 Technical Design of the Detector

2.1.1 Mechanical Design

The PROTO60 was designed with the aim to build a first standalone prototype, that represents as close as possible a subsection of the future PANDA barrel EMC. Fig. 2.1 indicates the region of the EMC, geometrically represented by the prototype. Thus, the PROTO60 consists of a 6×10 matrix of tapered PWO-II crystals with type 6 R/L geometry. The final barrel EMC will contain only four adjacent rows of crystals with the same type of geometry. Each single crystal of the prototype is equipped with one Hamamatsu LAAPD Type 8664-1010SPL, contained in a plastic socket and coupled to the end face with silicon oil (Fig. 2.3). The bare lead tungstate crystals (Fig. 2.2) are wrapped with the reflector material VM2000, taped with Mylarfilm and assembled to subunits of four crystals. Once taped together each package of crystals is inserted into tapered carbon alveoles (Fig. 2.4). The crystal quartettes are mounted to alveole inserts which contain as well the preamplifier type $SP883b$ for the 4 APD signals (Fig. 2.5).

In the case of the PROTO60, 6×10 of this single detectors are sourrounded by an aluminum box. Thin plates of copper are touching the aluminum box on each side. They are equipped with thin pipes for cooling liquid bend to an meander-like structure. In between the plates of copper and the outermost housing, made of PVC plastics, a thick layer of thermal insulation material is placed. On the front side is also a copper plate, but instead of a thick layer of insulation, a thermal shield was mounted. The shield is made of two aluminum plates with a short gap. They are supported by a carbon structure and the volume between the plates is evacuated, to avoid thermal conduction. The backside of the PROTO60 can be opened, to have fast access to the preamplifiers and readout backplanes. Fig. 2.6 shows the prototype from the back side, with only one mounted backplane, while in Fig. 2.7 all backplanes are in place.

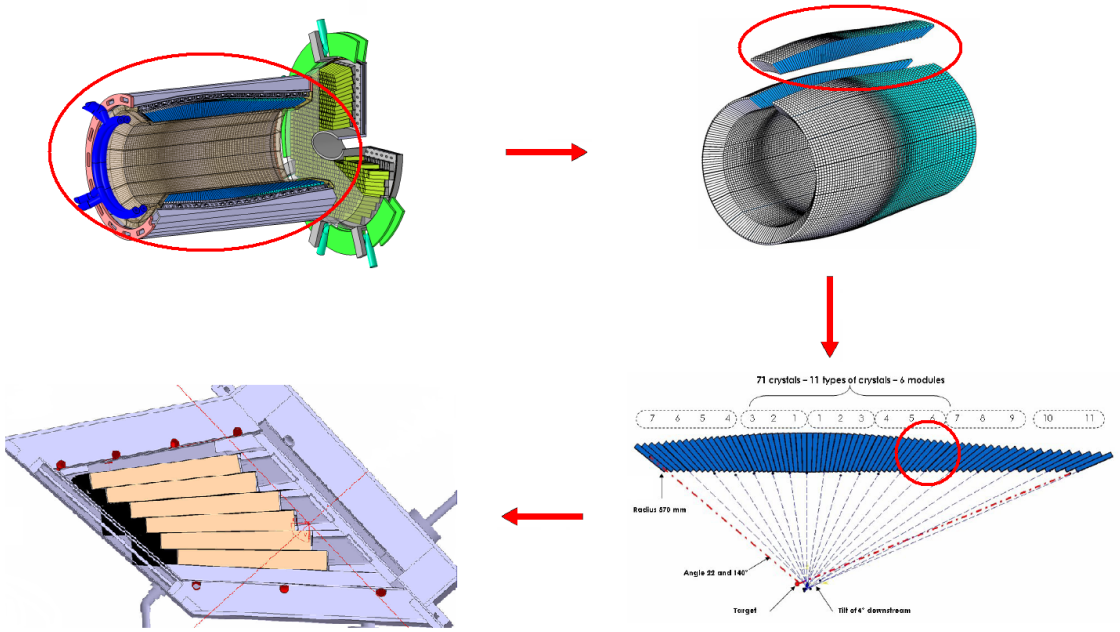

Figure 2.1: Schematic view of the EMC region represented by the PROTO60

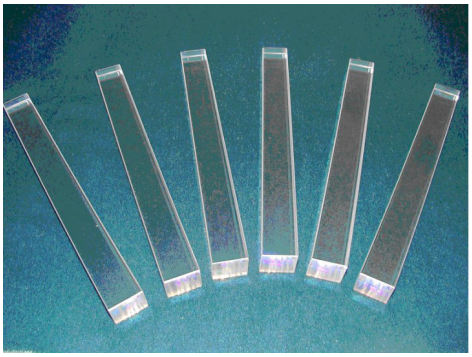

Figure 2.2: PWO-II crystals produced for the PANDA detector.

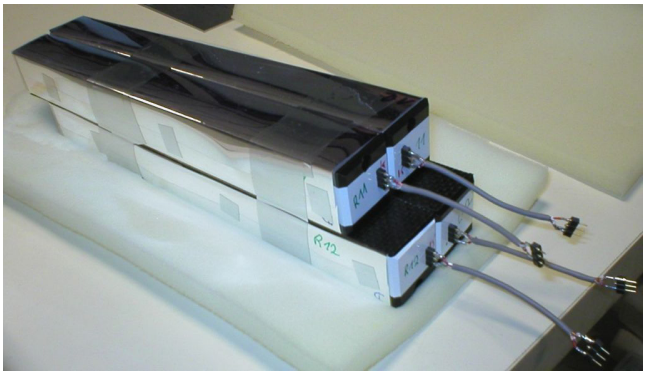

Figure 2.3: Staggered PROTO60 crystals wrapped with reflector material and equipped with LAAPDs.

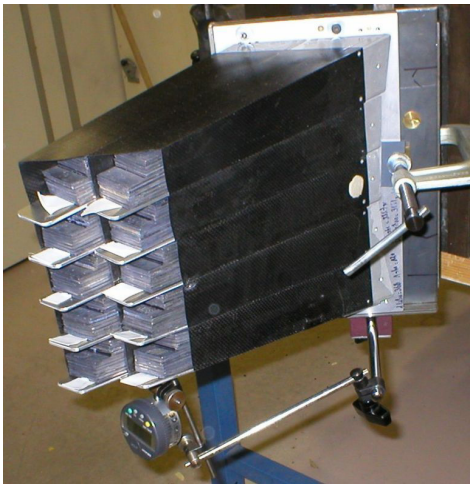

Figure 2.4: Carbon alveoles manufactured for PANDA during a test of mechanical stability.

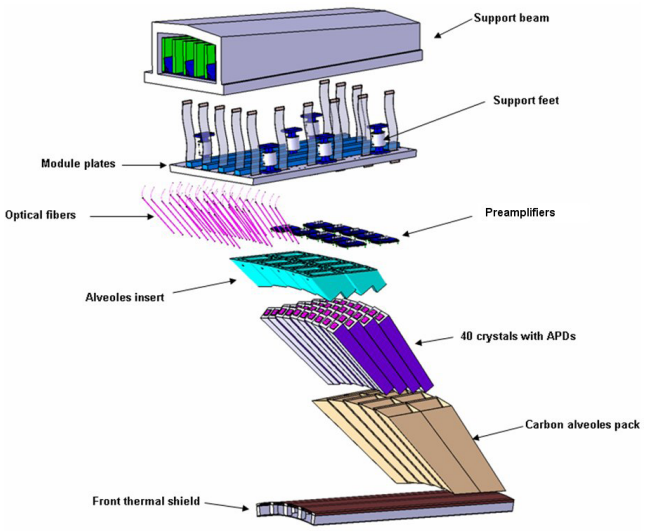

Figure 2.5: Exploded view of one subunit of the future barrel EMC.

Optical fibers, attached to the crystal rear face feed in light pulses to monitor any losses of scintillation light or electronics instabilities including the sensor. Due to the fact, that the readout devices are installed from the back, the crystals were numbered, following each row from left to right beginning with the top row. Adapted to the view seen on the front face of the prototype, this gives a numbering as indicated in Fig. 2.11. During operation, the PROTO60 is cooled down to $-25°C$ with a mixture of ethanol and water serving as cooling liquid. To avoid the formation of ice, the interior is additionally flooded with dry nitrogen, which significantly reduces the humidity.

2.1.2 Test Readout

Data Aquisition (DAQ) was performed with a chain of electronics, as sketched in Fig. 2.8. It consists of three main branches. The first one deals with the timing and trigger signals representing 16 selected tagger channels. A TRUE coincidence of the logical OR of all tagger channels with the signal of the third branch, which indicates the response of the central detector module (crystal 35), creates an event. Both signals were adjusted with discriminators in a way, that the timing of an event is governed by the central crystal. Additional types of events are created by testpulser or an external cosmic trigger. However, additional triggers were blocked when the readout boards were processing data. During each event a common start of all TDCs[1]

[1] **T**ime-to-**D**igital-**C**onverter

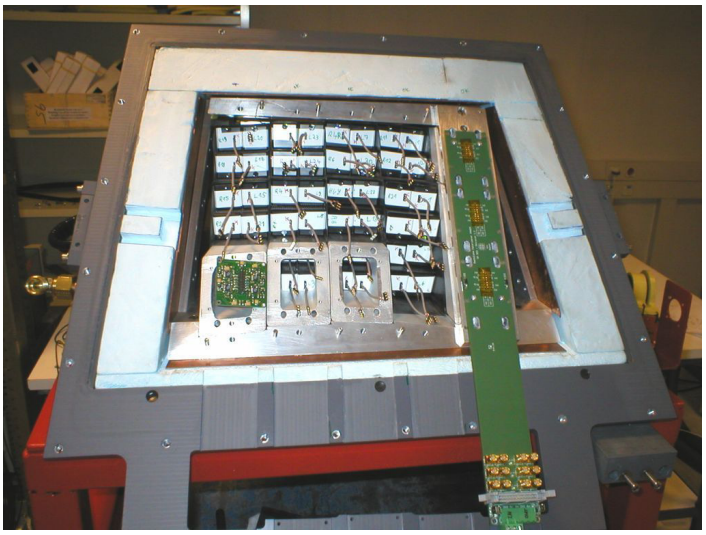

Figure 2.6: Photo of the PROTO60 seen from the rear side. One clearly recognises the 60 wrapped crystals and the cables from the LAAPDs. The whole structure is contained in a thermal insulated box.

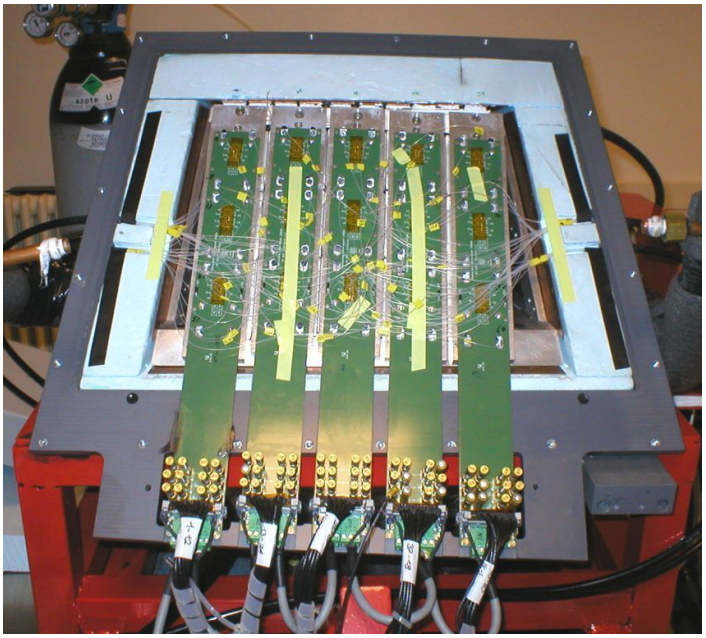

Figure 2.7: PROTO60 with all backplanes mounted.

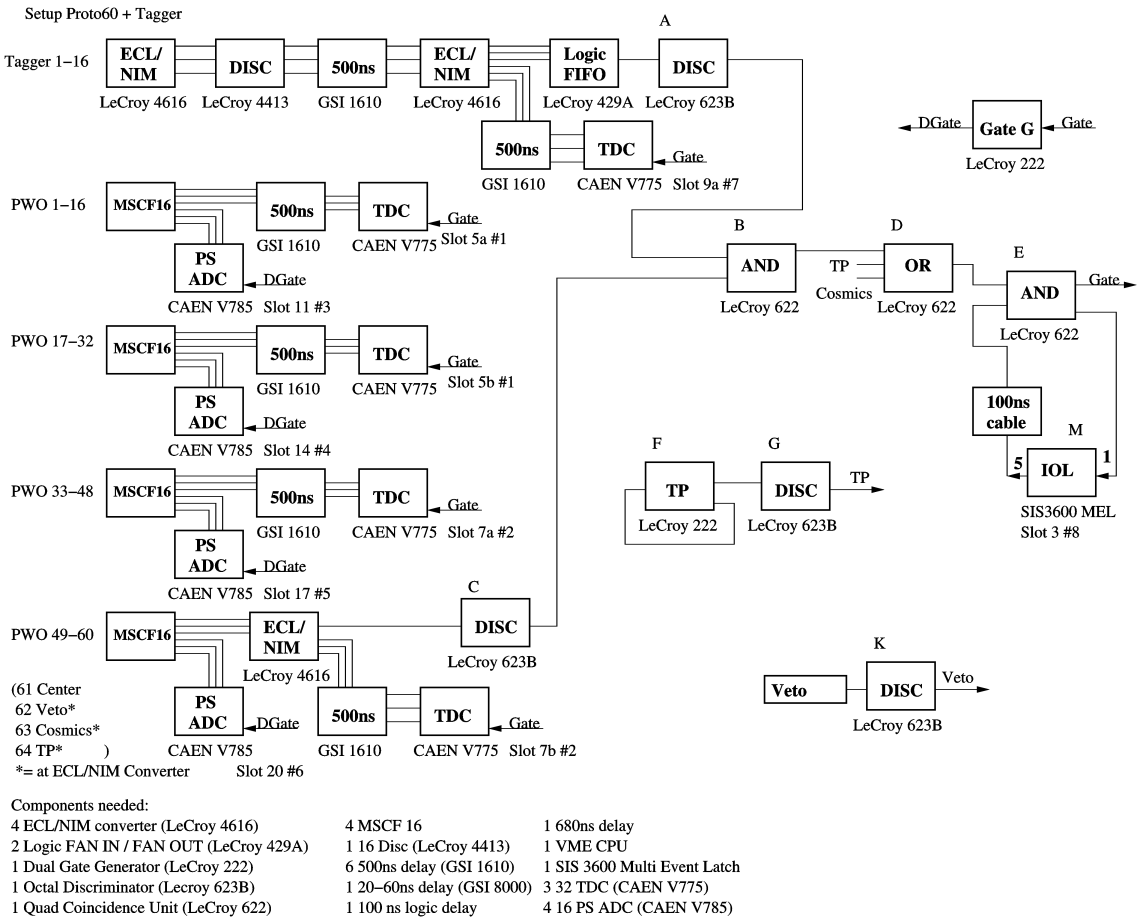

Components needed:

4 ECL/NIM converter (LeCroy 4616)	4 MSCF 16	1 680ns delay
2 Logic FAN IN / FAN OUT (LeCroy 429A)	1 16 Disc (LeCroy 4413)	1 VME CPU
1 Dual Gate Generator (LeCroy 222)	6 500ns delay (GSI 1610)	1 SIS 3600 Multi Event Latch
1 Octal Discriminator (Lecroy 623B)	1 20–60ns delay (GSI 8000)	3 32 TDC (CAEN V775)
1 Quad Coincidence Unit (LeCroy 622)	1 100 ns logic delay	4 16 PS ADC (CAEN V785)

Figure 2.8: Layout of the DAQ electronics of the PROTO60 which was used to measure the data analysed in this thesis.

was performed. They are stopped individually by the signals from CFDs[2] included in MSCF16 modules. These devices handle 16 detector channels and are able to process the output signals of the preamplifiers in two different ways. After a common amplification the input signal is split and fed into either a spectroscopy amplifier or a CFD to deduce an appropiate timing. The MSCF16 output of each branch is read out by a corresponding 16 channel PS-ADC[3], which digitizes the pulse height of the signal in a common time gate of 1-2 μs for each event.

If an event is readout under the conditions given above, digitised information of the deposited energy for each crystal of the PROTO60 is stored. In addition, the timing information of the selected tagger channels, of crystals with energy deposition above the CFD energy threshold and of several external devices like the testpulser and the veto are also stored event wise in list mode.

2.2 Test Measurement Performance

The test measurement analysed in this thesis was performed at the MAMI[4] accelerator facility in Mainz, Germany providing an electron beam up to an energy of 1507 MeV. First, a sequence of three racetrack-microtrons (RTM, Fig 2.9) accelerates electrons up to 855 MeV energy. These microtrons consist in principle of two dipole magnets with constant magnetic field, which bend the tracks of electrons by 180 degrees. The radius of curvature rises with the energy of the electrons. Despite of this, the combination of two magnets results in the fact, that on one straight section of the microtron the electrons always pass along the same track, where they are accelerated by a linear accelerator operating with a constant frequency of 2.45 GHz.

In a second stage, the electrons can be accelerated further by a harmonic doublesided microtron (HDSM, Fig. 2.10), which provides a maximum beam energy of 1507 MeV. It consists of four dipole magnets, which bend the electron track in each corner by only 90 degrees. In that case it is possible to install two acceleration lines. One of the major advantages of these microtrons, next to the simplicity and robustness, is the opportunity to operate in continuous wave mode, which minimizes luminosity fluctuations, allows to produce a beam of tagged photons and is the ideal condition for coincidence measurements.

The device suited for this purpose is the so called Mainz-Glasgow-Tagger, illustrated in Fig. 2.13. The high energy electrons are impinging a thin metal foil and generate bremsstrahlung due to deacceleration in the radiator. The magnetic field of a dipole

[2] **C**onstant-**F**raction-**D**iscriminators
[3] **P**eak **S**ensing **A**nalog **D**igital **C**onverter
[4] **MA**inzer **MI**crotron

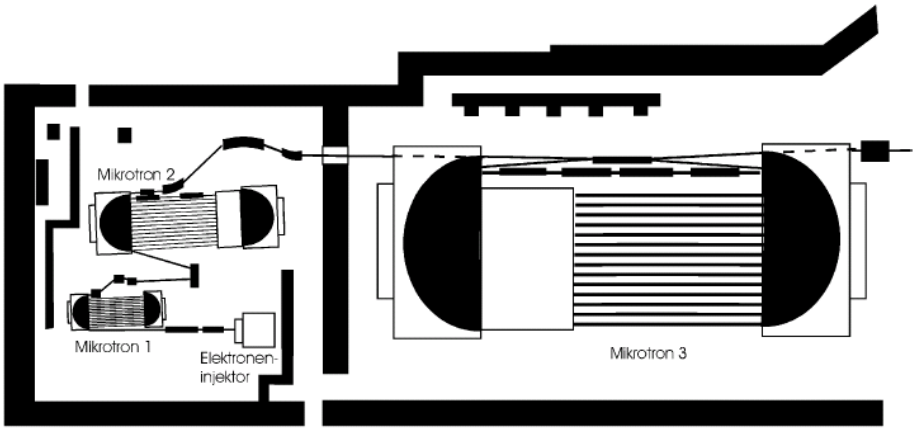

Figure 2.9: Sequence of the three MAMI racetrack-microtrons to accelerate electrons up to an energy of 855 MeV.

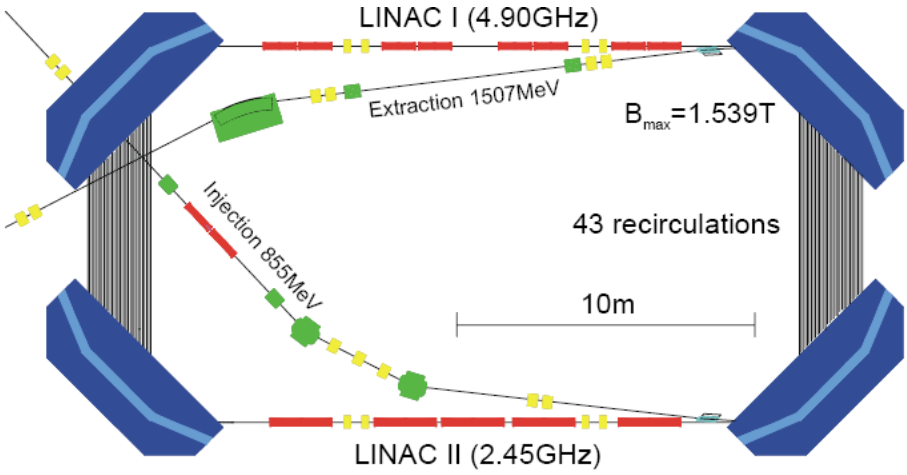

Figure 2.10: Schematic view of the doublesided harmonic microtron at MAMI. The maximum electron beam energy, achievable with this device corresponds to 1507 MeV [MKA$^+$08].

disperses the electron tracks according to their final energy. By the position sensitive detection of this electrons with 352 slightly overlapping plastic scintillator detectors with a single width of 24 mm, the radius of curvature and the corresponding remaining momentum p_e of the electron are determined. The corresponding energy of the produced photon E_γ is given by the difference of the beam energy E_{Beam} and the remaining energy of the electron $E_e = \frac{p^2}{2m_e}$.

$$E_\gamma = E_{Beam} - E_e \tag{2.1}$$

Knowledge of the coincident tagger channel allows to calculate E_γ with an uncertainty ΔE_γ reaching from 2.06 MeV for the lowest channel to 4.16 MeV for the highest, respectivley. The time resolution of a single channel corresponds to 170 ps [MKA+08].

The lateral profile of the energy marked photon beam is governed by the angular distribution of the bremsstrahlung, which is emitted in a cone with opening angle Θ approximated by

$$\Theta = \frac{p_{Beam}}{m_e} \tag{2.2}$$

The use of a set of dense collimators allows to limit the beam shape. However it is difficult to determine the true intensity profile within the beam spot. Thus for the experiment an estimation had to be made.

The test of PROTO60 was performed in February 2009. Fifteen different tagger channels with photon energies ranging from 150 MeV to 1450 MeV were selected. Detailed values are given in Table 2.1. The prototype was mounted on a steel frame and adjusted in a way, that its longitudinal symmetry axis was parallel to the beam direction. Stepper motors allowed a positioning relative to the beam with a precision of 1 mm in both, x- and y-direction. Photos of the setup are shown in Fig. 2.12. Four runs with comparable statistics were performed with the photon beam impinging on three different locations, displayed in Fig. 2.11. In addition, run number four was performed with a lead sheet in front of the veto detector and thus in front of the center of the prototype. The lead had a thickness of 2 mm which corresponds to 36% of radiation length X_0. The dynamic range of the energy readout of the individual detector module was adjusted to 200 MeV. For crystal 35, where the beam was impinging, the amplifier output was passively attenuated (15 db) to cover the full energy range. For the second and third run, were, according to Fig. 2.11, the beam beam was hitting outside the center of this crystal, also crystal 36 was equipped with an attenuator.

2.3 Energy Calibration

The calibration was performed by measuring cosmic rays in two separate runs and even during the experiment, distinguished from other events by a cosmic trigger. To

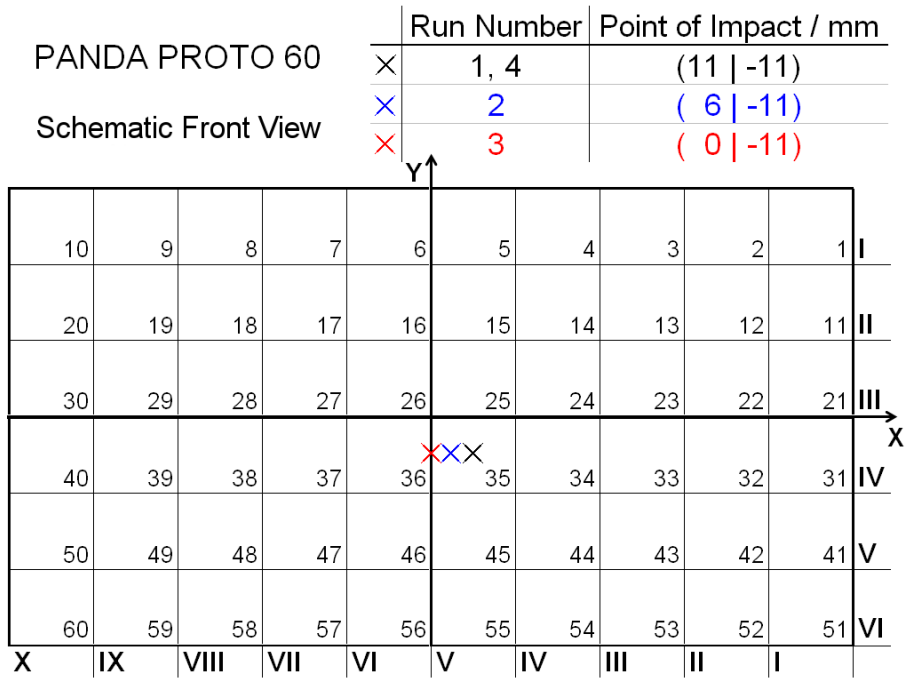

Figure 2.11: Schematic front view of the PROTO60. The colored crosses mark the point of impact of the photon beam. Also the coordinates in x- and y-direction are given in mm.

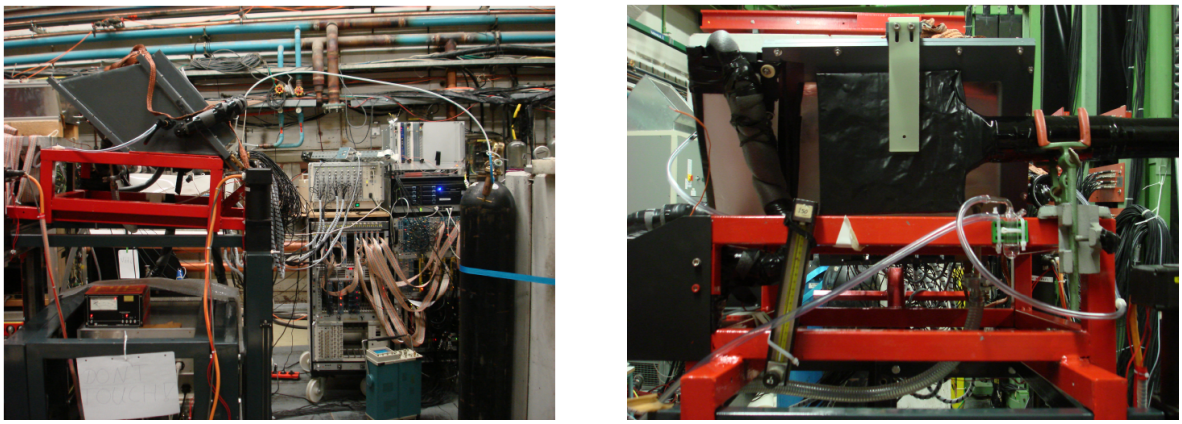

Figure 2.12: Side view of the PROTO60 with photon beam coming from the left (left) and front view (right) during the test run in February 2009.

TDC Number	Photon Energy E_γ in MeV
1	1441.06
2	1356.89
3	1257.31
4	1156.56
5	1057.70
6	956.16
7	857.98
8	756.58
9	657.34
10	556.97
11	456.26
12	355.88
13	256.41
16	187.99
14	158.31

Table 2.1: Overview of the selected tagger channels and the corresponding photon energy E_γ.

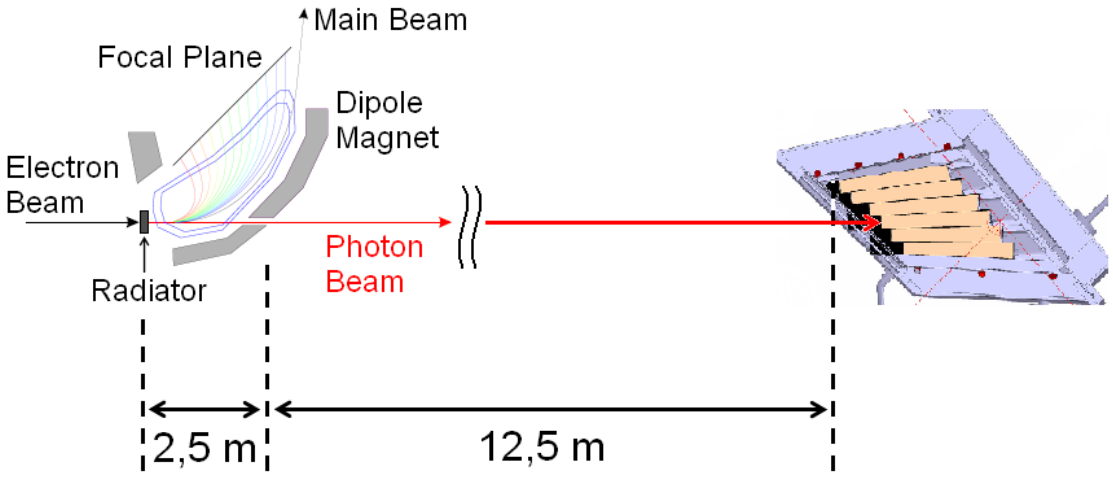

Figure 2.13: Schematic view of the setup with the tagger (left) and the PROTO60 (right). The picture is not to scale.

reduce passlength variations, only those events were selected, where the cosmic rays passed crystals in the same column. The peak caused by minimum ionizing particles, i.e. cosmic muons, was fitted with a Landau function (Fig. 2.14). In addition, the

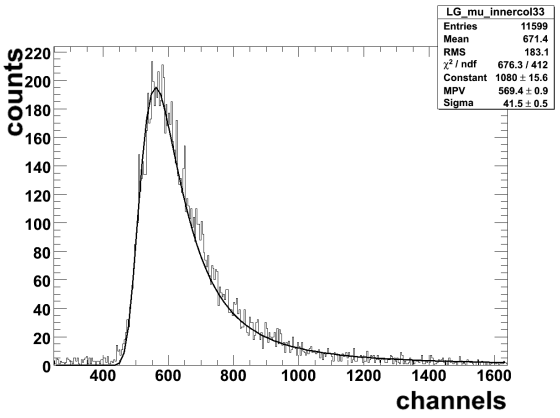

Figure 2.14: Example of minimum ionizing peak, caused by cosmic muons, fitted with a Landau function [Mor09].

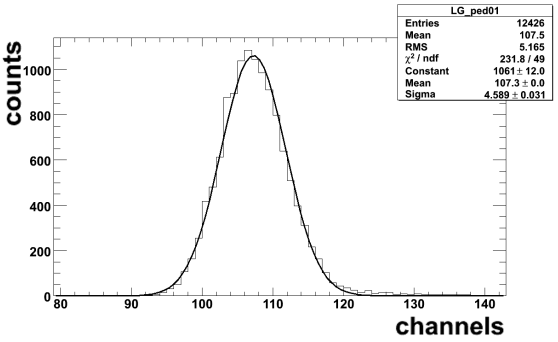

Figure 2.15: Spectrum of the pedestal, fitted with a Gaussian function [Mor09].

mean ADC channel P_{Ped} of the pedestal was determined by fitting with a Gaussian function. It represents the true zero point of the pulse height spectrum. The pedestal was continuously readout by using a testpulser which provided gate signals. Knowing the mean ADC channels of pedestal P_{Ped} and muon minimum ionizing peak P_{Muon} for each crystal of the prototype, it was possible to perform a relative calibration by dividing channel number of a energy measurement P by the difference of P_{Muon} and P_{Ped}. In order to obtain an absolute calibration the energy deposition of the muons had to be estimated. According to [Ams08], the average stopping power in PWO amounts to $10.2\frac{\text{MeV}}{\text{cm}}$, while the average passlength across a crystal of the PROTO60 amounts to approximately 24 cm, as illustrated in Fig. 2.16. This gives an average energy deposition of 24.5 MeV per crystal due to cosmic muons. Deviations from this value, because of different crystal sizes, are below 0.27% and were neglected. Altogether, the energy content of one ADC channel, according to this calibration procedure [Mor09], is given by

$$E_{Ch} = \frac{24.5 \text{ MeV}}{P_{Muon} - P_{Ped}}. \tag{2.3}$$

On the base of the energy calibration described in this section, the data analysis described in chapter 3 was performed.

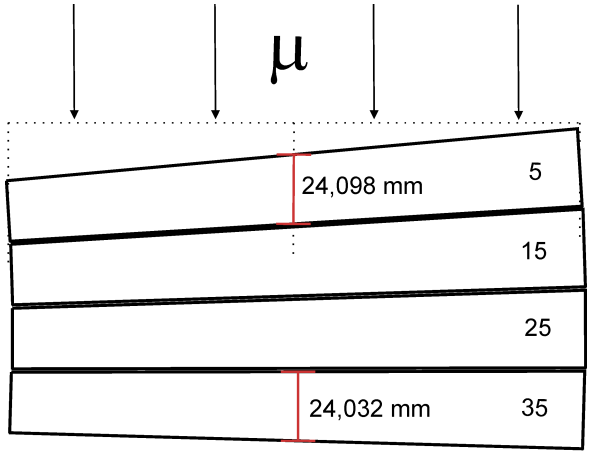

Figure 2.16: Schematic drawing of the pass track of comsmic muons through one column of the PROTO60.

Chapter 3

Data Analysis

3.1 Shower Energy Reconstruction

3.1.1 Line Shapes

The first step after energy calibration was to investigate the ability of the PROTO60 to reconstruct the energy of the electromagnetic shower of the measured high-energy photons. If not pointed out explicitly, the analysis is always based on data acquired with the beam impinging in the center of crystal 35, therefore often called 'central crystal'. For reconstruction only events were chosen, when the veto detector in front of the prototype was not responding. This detector is only sensitive to charged particles. Therefore, under this condition events are filtered out, when conversion of the incoming photons has occurred somewhere before the PROTO60. Furthermore, a crystal of the PROTO60 is considered, when a deposited energy above a software energy threshold E_{xtl} was recorded. By systematic variation the most optimum value of E_{xtl}, minimizing the noise contribution, was determined as $E_{xtl} = 0.75$ MeV. The width of the noise peak in the energy spectrum was determined by fitting with a Gaussian to be $\sigma_{Noise} = 0.25$ MeV. This relation $E_{xtl} = \sigma_{Noise}$ is in accordance with the expectations of the TDR [PAN08].

Applying this threshold, the line shapes of the central crystal, and the sum of all single crystal energies in an array of 3×3, 5×5 crystals and in the whole 6×10 matrix of the PROTO60 are plotted in Fig. 3.1 at two extreme incident photon energies of 158 MeV and 1441 MeV, respectively. It shows that the energy is also well reconstructed by taking into account 5×5 crystals, while the energy sum of the 3×3 array is slightly shifted to lower energies. This occurs most likely due to transversal distribution of the electromagnetic shower. To determine the width σ_E and mean value E_0 of an energy

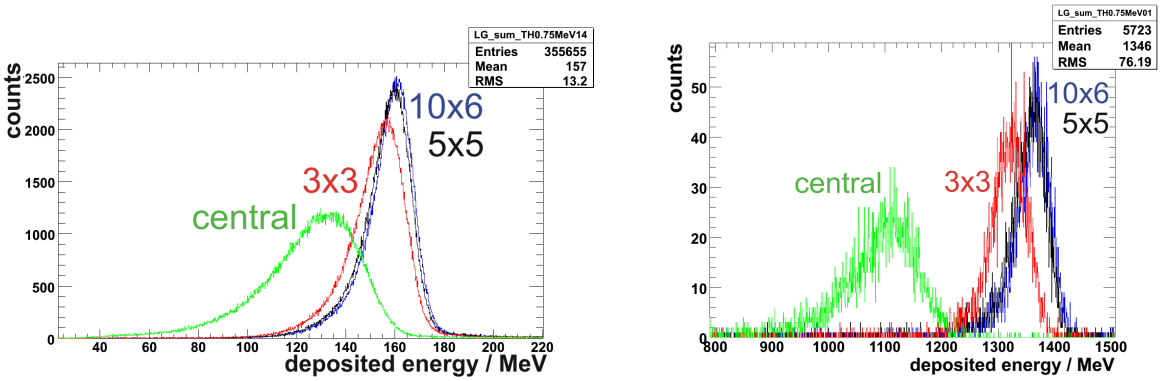

Figure 3.1: Line shapes of different arrays at an incident photon energy of 158 MeV (left) and 1441 MeV (right) [Mor09].

sum, each distribution was fitted with the so called Novosibirsk function Eq. 3.1.

$$f(E) = Ae^{-\frac{\ln[1-\Lambda\tau(E-E_0)]^2}{2\tau^2}+\tau^2} \tag{3.1}$$

$$\Lambda = \frac{\sinh(\tau\sqrt{\ln 4})}{\sigma\tau\sqrt{\ln 4}} \tag{3.2}$$

This Function takes into account the low energetic tail, caused by shower fluctuations and losses, by introducing an additional parameter τ. It's width σ is, analog to the Gaussian function given by $\sigma = \frac{\mathrm{FWHM}}{2.36}$. FWHM means **F**ull **W**idth at the **H**alf of the **M**aximum peak heigth. An example for such a fit is displayed in Fig. 3.2. By extracting the fit parameters several other features concerning the energy reconstruction can be proven, as described in the following section.

3.1.2 Energy Response

The linearity of the energy response of PROTO60 is investigated by plotting the mean energy sum versus the incident photon energy, as shown in Fig. 3.3. The same is done for the deposited energy in the central crystal. The energy dependence of the relative energy resolution $\frac{\sigma_E}{E}$ is displayed in Fig. 3.4. Beside the parametrization corresponding to the TDR the data was also fitted with a function according to Eq. 1.10, which results in the following expression:

$$\frac{\sigma_E}{E} = \sqrt{(1.55\%)^2 + \left(\frac{1.85\%}{\sqrt{E}/\mathrm{GeV}}\right)^2 + \left(\frac{0.40\%}{E/\mathrm{GeV}}\right)^2} \tag{3.3}$$

In addition, it is important to point out, that the energy resolution depends also on the point of impact of the incident photon. In Fig. 3.5 the energy resolution is plotted

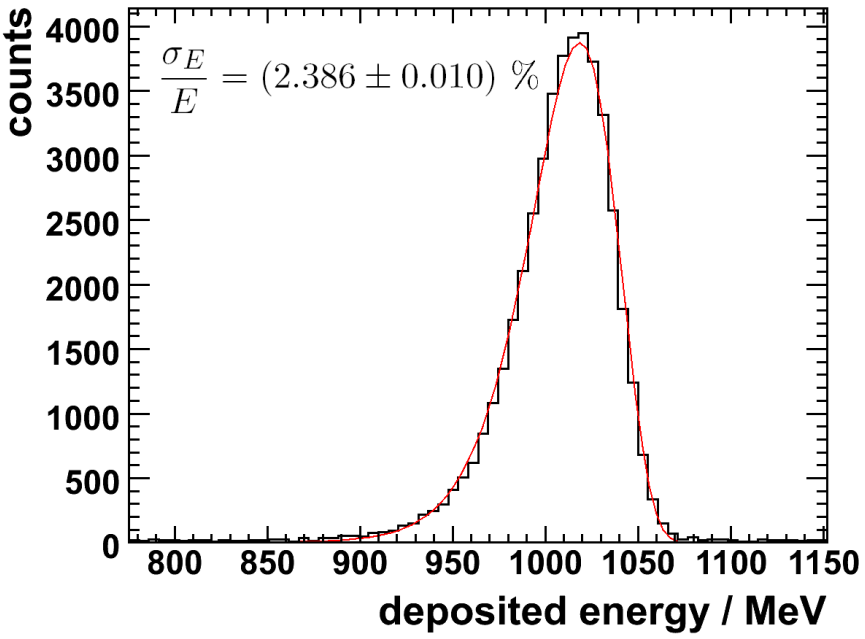

Figure 3.2: Novosibirsk fit of the energy sum peak for the whole detector at an incident photon energy of 1057 MeV.

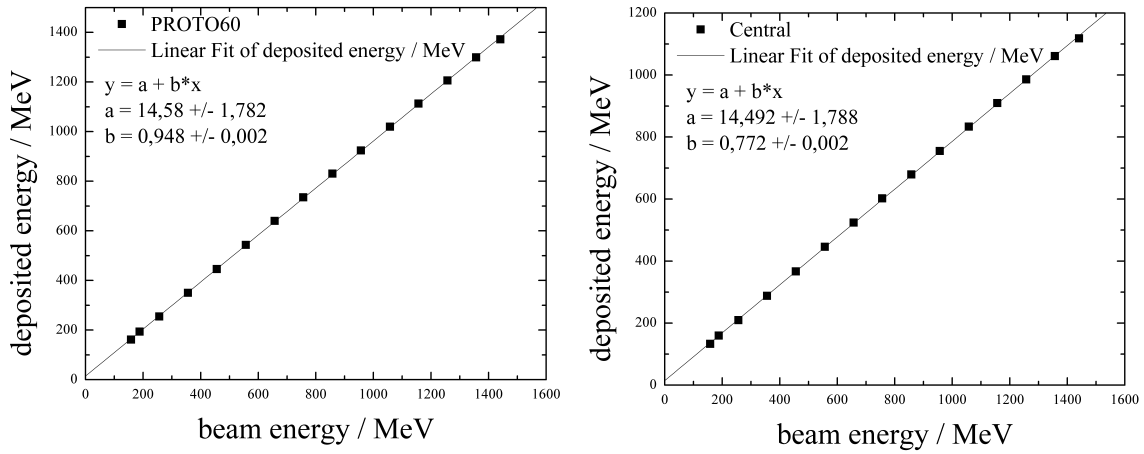

Figure 3.3: Linearity of the energy response for the energy sum (left) and the central crystal (right) [Mor09].

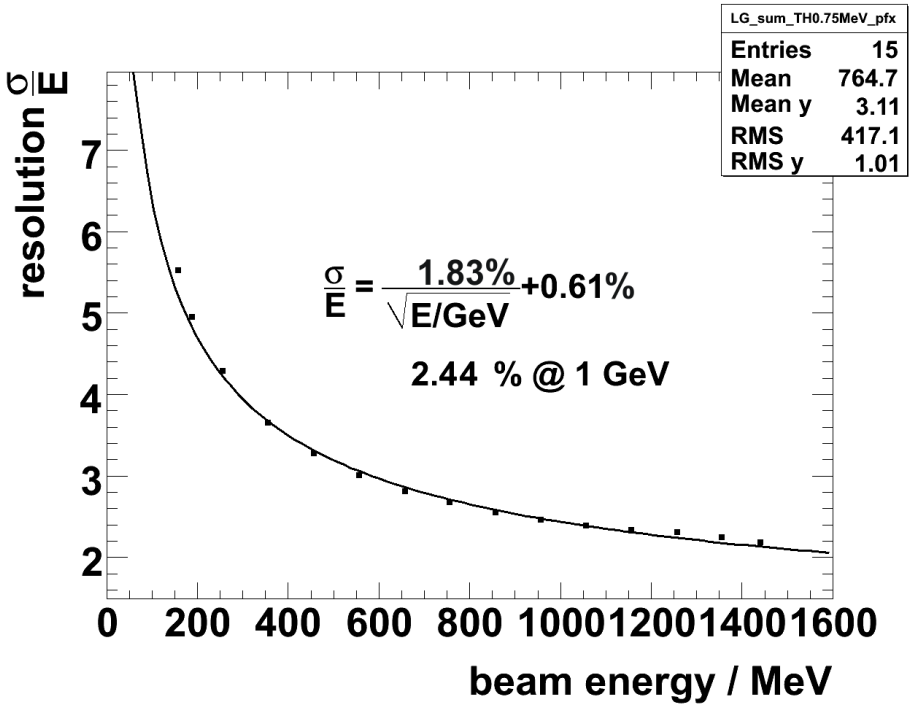

Figure 3.4: Energy dependence of the relative energy resolution at a single crystal threshold of 0.75 MeV [Mor09].

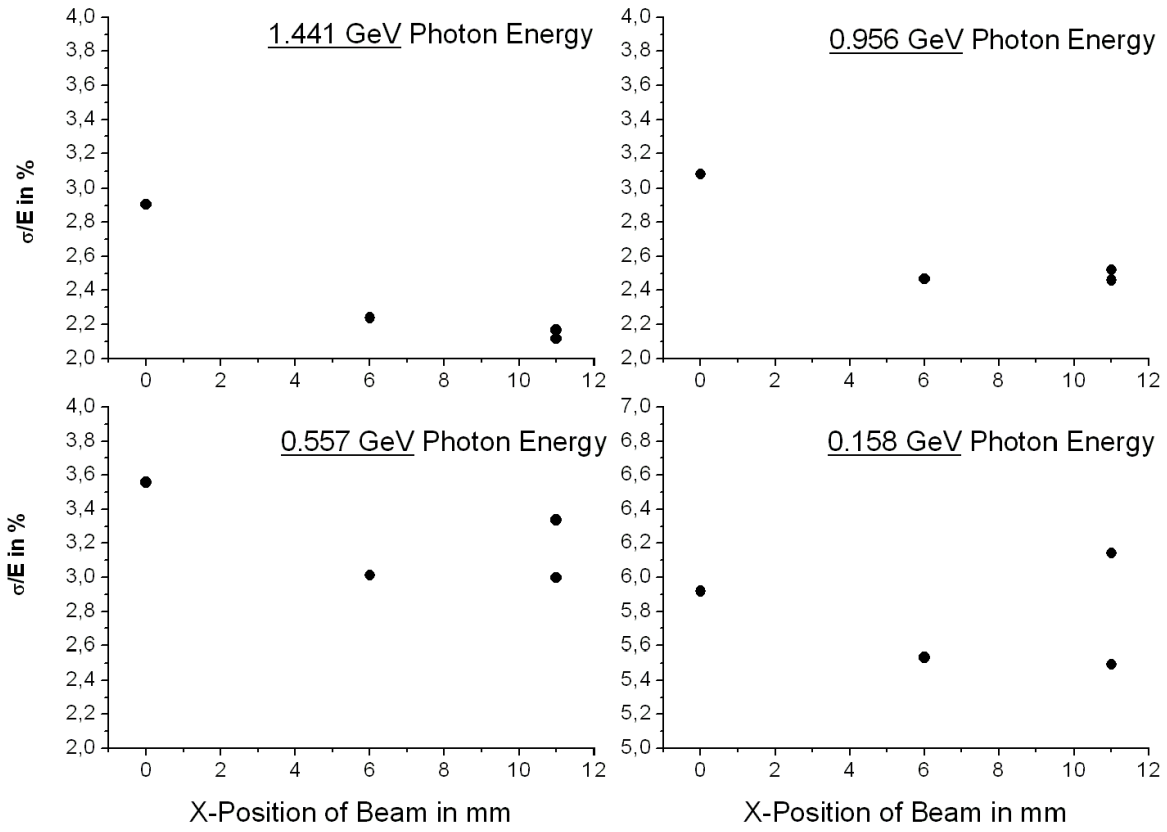

Figure 3.5: Relative energy resolution plotted versus the position of the beam. The split in resolution between the two runs in central position indicates veto inefficiencies.

versus the position of the beam for four selected incident energies. The resolution is reduced with growing distance to the center of a crystal (at 11 mm).

The run in central position showing a reduced resolution was performed with a lead sheet mounted in front of the PROTO60. Because of the fact that the veto detector was not identifying charged particles with sufficient efficiency, a suppression of conversion events was not completely guaranteed. Therefore, the measured resolution for this run is deduced from a mixture of events with and without conversion. Hence, the degradation in resolution, which is increased at lower energy, is caused by conversion in the lead sheet.

3.2 Time Resolution

3.2.1 Difficulties

A determination of the time resolution of the PROTO60 is challenging for several reasons. The timing information was started by the event and stopped individually by each crystal. Therefore, the central crystal was self triggering (compare Section 2.1.2) and delivers a sharp spike. The width of the individual time spectra is determined by both, the time resolution of the center and the individual crystal. As pointed out in Section 2.2, the time resolution of an individual tagger channel is significantly better than the expected single crystal resolution and its contribution can be neglected. Therefore, by measuring the time resolution of the single tagger channels with the described readout, it is possible to determine the contribution due to the time resolution of the central crystal.

The deduced time information of the crystal modules is deteriorated electronically by the walk effect, a time shift due to a trigger dependence on signal amplitude. The intrinsic signals from the tagger can be considered as walk-free, because all signal amplitudes, caused by minimum ionizing electrons, are similar. Fig. 3.6 shows a clear non-linearity of the uncorrected time information. These effects occur in spite of the fact that CFDs were used for proper timing. Nonetheless, their energy thresholds for each channel were not aligned accurately, since the experiment originally was not aiming at the determination of time resolution and took place in a very strict time schedule. Moreover, for the used MSCF16 modules a remote control of thresholds is not available and a justification accordingly becomes difficult and time consuming.

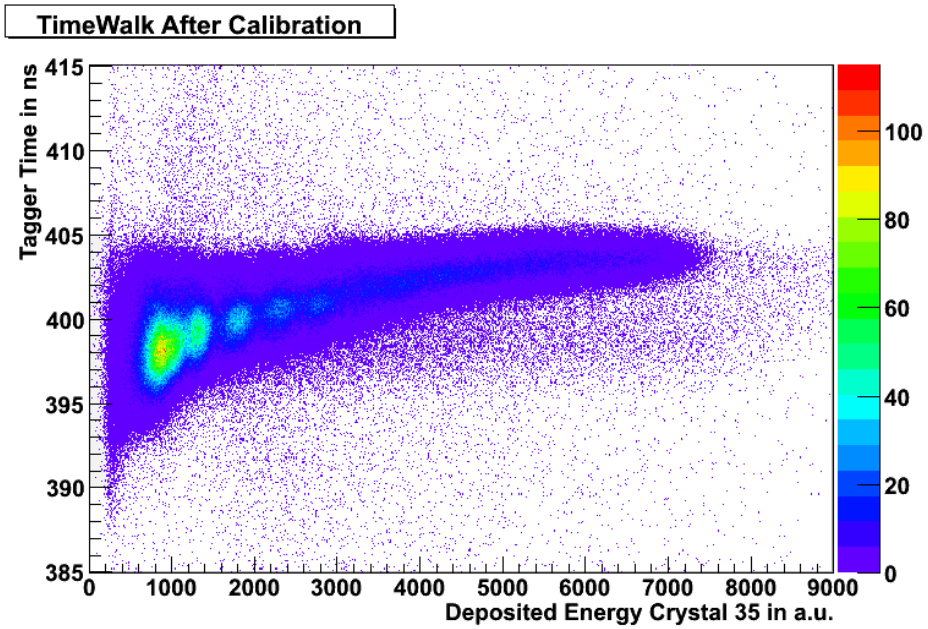

Figure 3.6: Diagram of the already calibrated tagger time vs the deposited energy in the central crystal. A clear nonlinearity is visible.

3.2.2 Linearisation

In order to linearize the time information, the raw TDC channel information from the 15 tagger channels had to be calibrated absolutely. In a first step the time of each tagger channel was plotted versus the deposited energy in the central crystal as displayed in Fig. 3.7. Adjacent tagger channels, e.g. 8 and 7, were overlapping in the range of the deposited energy. There, the relative shift to each other could be determined and removed by comparing the time of both channels at the same energy. This procedure was executed consecutively for all tagger channels, beginning with the lowest incident energy, channel 14. To obtain absolute time values, each TDC channel was slightly smeared out with a random function and multiplied with the corresponding calibration factor of 0.17 ns per channel. This value was determined as indicated in Fig. 3.8. A testpulser signal was digitized by the TDC with and without a delay of 16 ns. The delay time divided by the distance of the peaks, gives the time calibration factor. Fig. 3.6 shows the calibrated time in ns of all channels plotted against the deposited energy in crystal 35. The obtained correlation allowed to parametrize the contribution due to the CFD-walk. In a first step the diagram in Fig. 3.6 was divided into energy slices including 4 adjacent bins. The time content was projected and then fitted with a Gaussian function to determine the mean position. The resulting points are illustrated in Fig. 3.9. Based on the good experiences of the

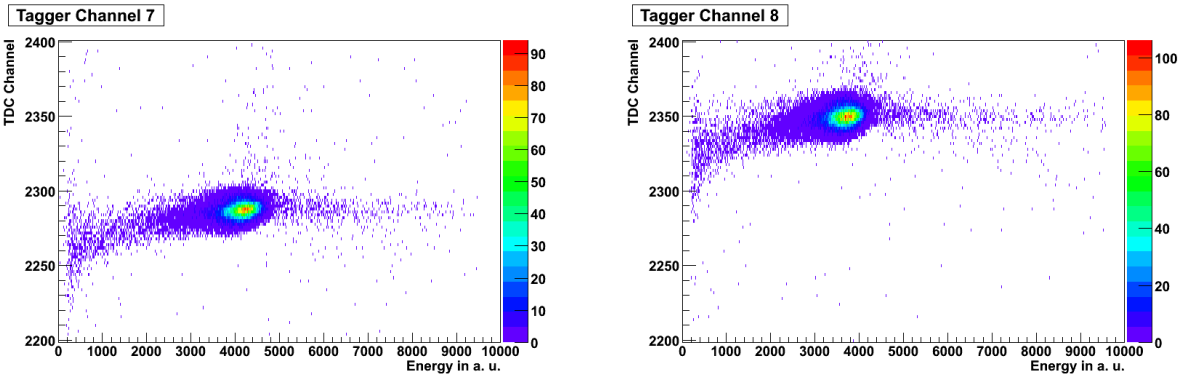

Figure 3.7: Time walk spectrum of two adjacent tagger channels. One energy bin in the overlap region was chosen to determine the time offset to each other.

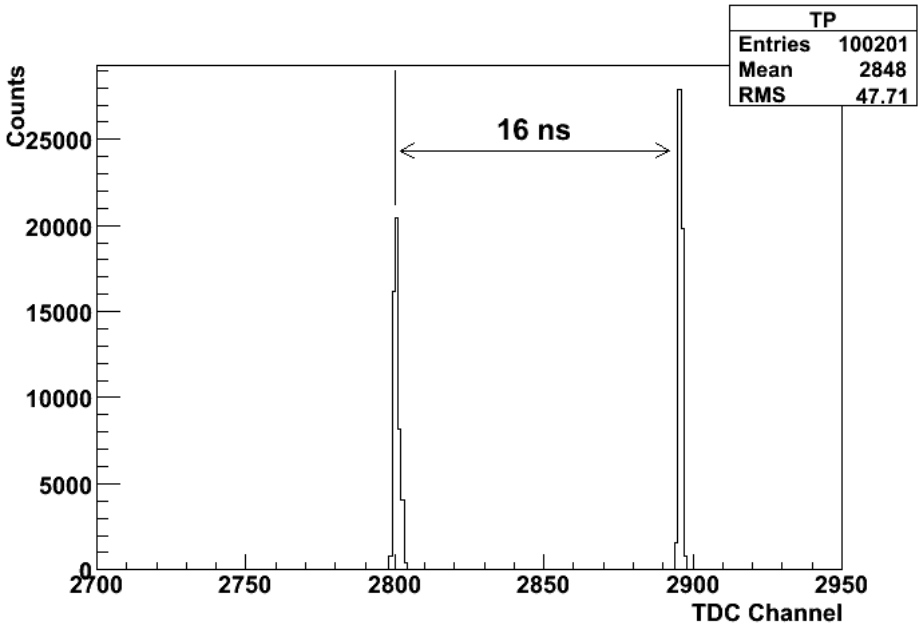

Figure 3.8: Prompt time signal of the testpulser digitized by the TDC with (right peak) and without a delay of 16 ns (right peak).

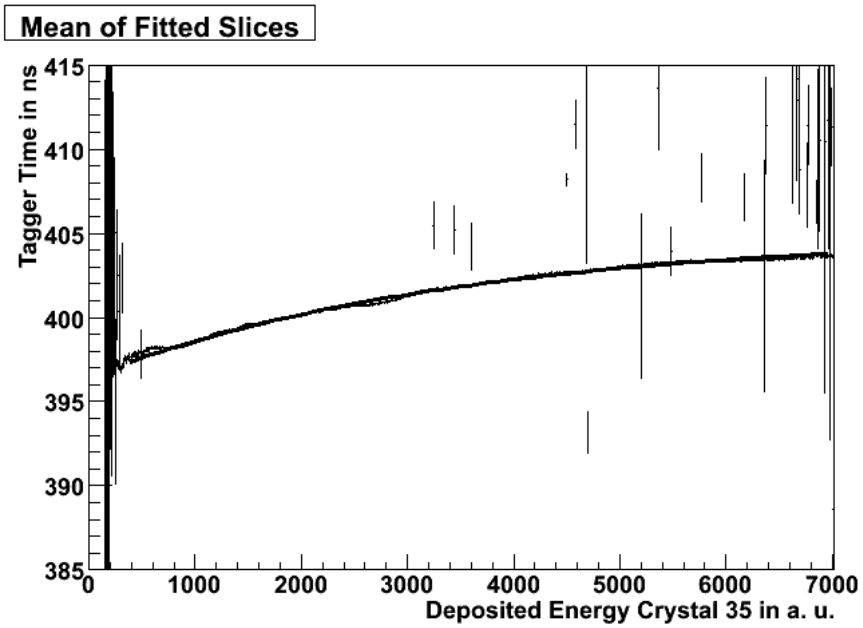

Figure 3.9: Mean value of the projected energy slices fitted with a Gaussian function.

TAPS group Giessen, Eq. 3.4

$$t(E) = A \cdot e^{B \cdot \sqrt{E} + C \cdot E} + D \tag{3.4}$$

was chosen for parametrisation. This function describes the measured time t in dependence on the deposited energy E. A, B, C and D are free parameters. Fitting Fig. 3.9 with Eq. 3.4 results in Eq. 3.5.

$$t(E) = -8.67320 \text{ ns} \cdot e^{-1.04279 \cdot 10^{-3} \cdot \sqrt{E} - 2.73275 \cdot 10^{-4} \cdot E} + 4.04973 \cdot 10^2 \text{ ns} \tag{3.5}$$

An overlay of this curve with Fig. 3.6 is displayed in Fig. 3.10. The parametrisation of the time walk allows an eventwise correction leading to the result in Fig. 3.11.

3.2.3 Achieved Resolutions

After applying the corrections described in the previous section, it was possible to determine the time resolution as a function of energy. For this purpose the time spectrum of each tagger channel was plotted and fitted with a Gaussian function, as illustrated in Fig. 3.12. The deduced widths σ_t plotted vs. the deposited energy is visualized in Fig. 3.13. The parametrization is expressed in Eq. 3.6 and was obtained

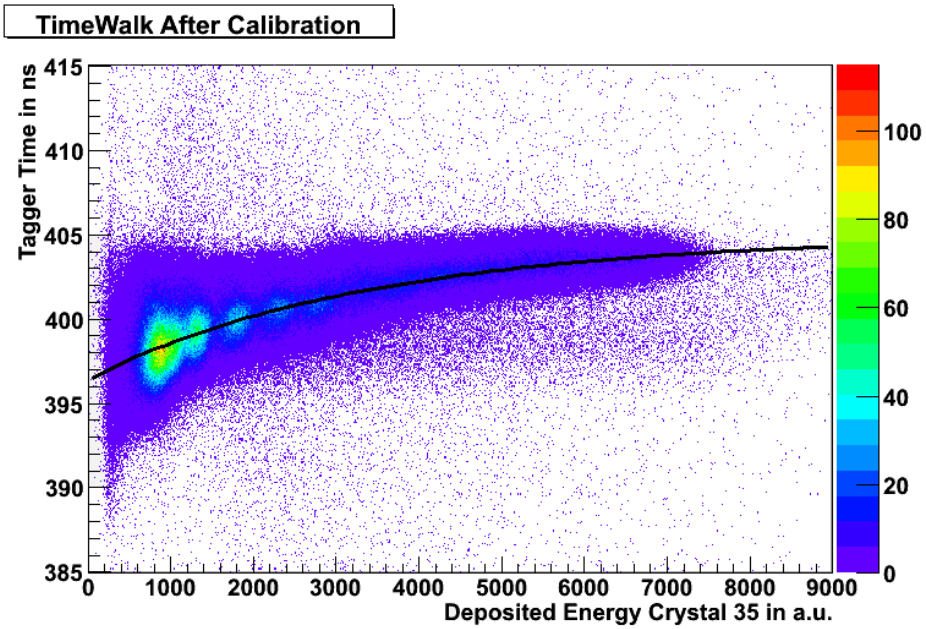

Figure 3.10: Calibrated tagger time vs. the energy deposited in crystal 35. The black line represents a fit of the mean time of slices of 5 adjacent energy bins with the function in Eq. 3.5.

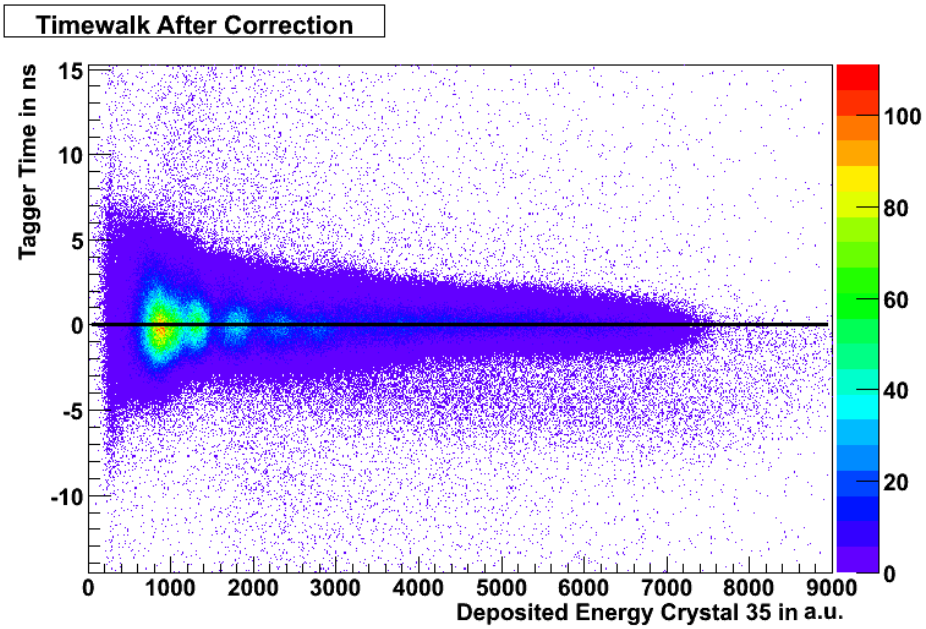

Figure 3.11: Time walk corrected time vs. the energy deposited in crystal 35. The black line represents a fit of the mean time of slices of 4 adjacent energy bins with a constant.

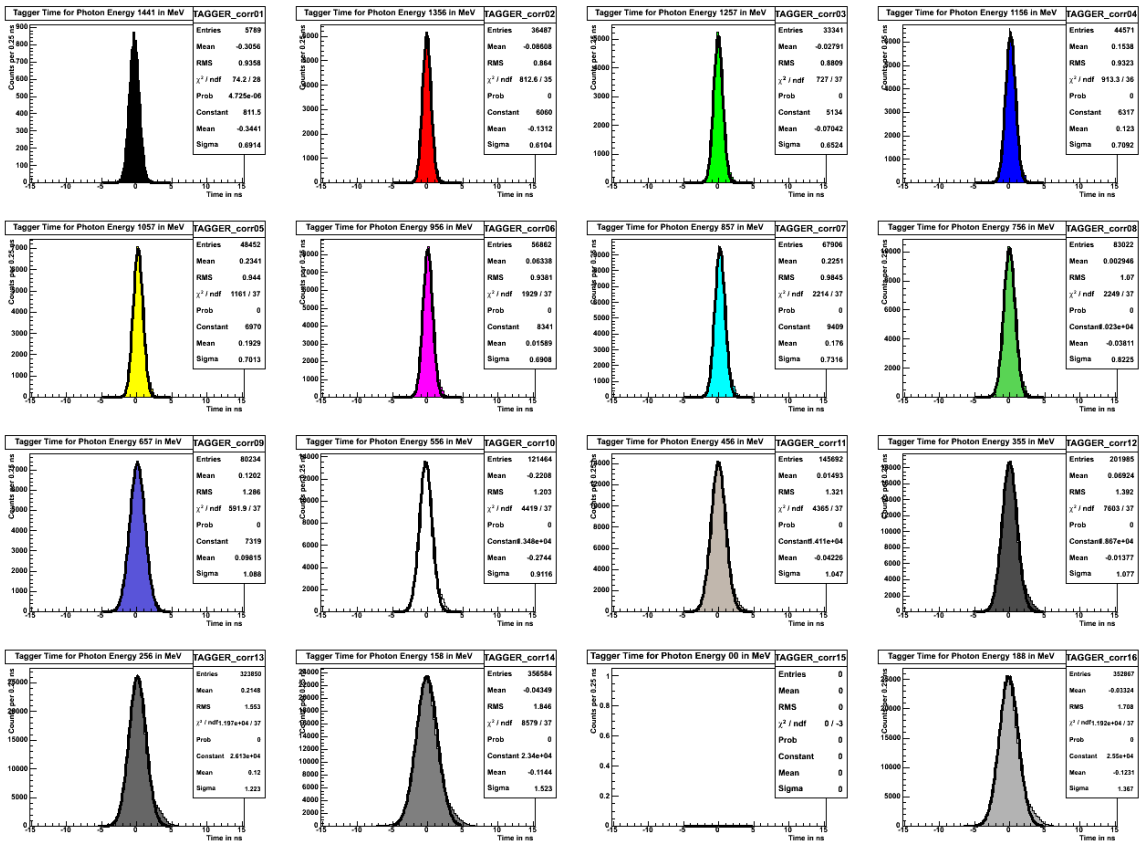

Figure 3.12: Overview of the time spectra of the 15 tagger channels, starting with channel 1 in the upper left corner. All spectra are fitted with a Gaussian function to determine their width.

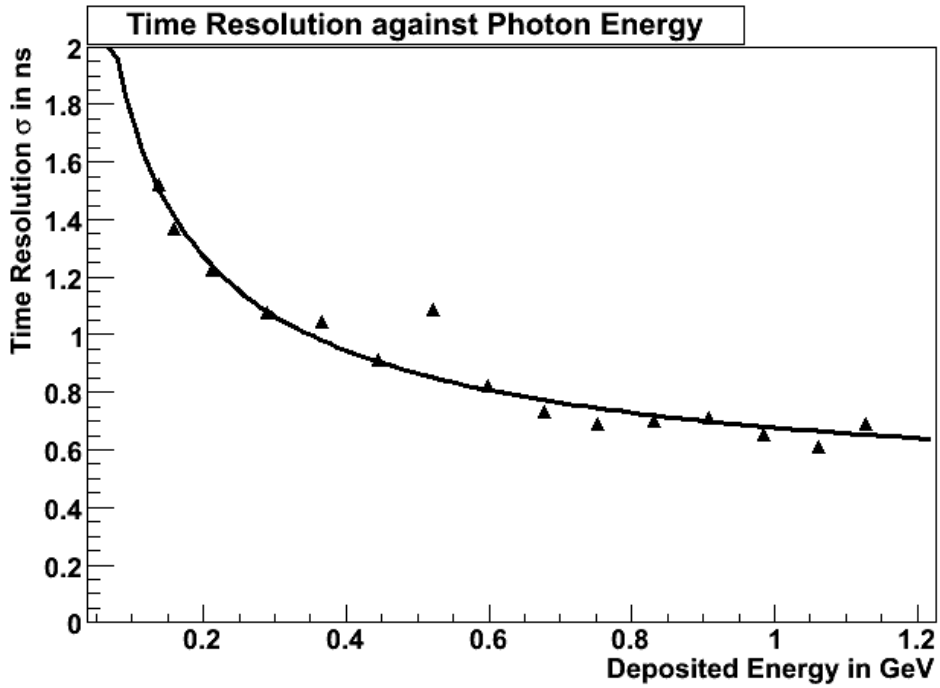

Figure 3.13: Energy dependence of the time resolution fitted with a three parameter function. The resolution at 1 GeV amounts to 0.678 ns.

by fitting.

$$\sigma_t = \sqrt{(412\text{ ps})^2 + \left(\frac{540\text{ ps}}{\sqrt{E/\text{GeV}}}\right)^2} \tag{3.6}$$

This corresponds to 680 ps at 1 GeV. Under the assumption, that the measured time resolution σ_t is equal to the quadratic sum of the intrinsic resolution of the central $\sigma_{central}$ and tagger σ_{tagger}

$$\sigma_t^2 = \sigma_{central}^2 + \sigma_{tagger}^2 \tag{3.7}$$

one obtains

$$\sigma_{central} = \sqrt{\sigma_t^2 - \sigma_{tagger}^2} = 660\text{ ps} \tag{3.8}$$

As expected, the contribution of the tagger detector is negligible. Therefore the σ_t is indeed governed by $\sigma_{central}$.

The impact of the performed time walk correction is mainly visible in the overall time resolution. Fig. 3.14 displays the time distributions of the calibrated tagger time still including walk effects and the time distribution after the walk correction.

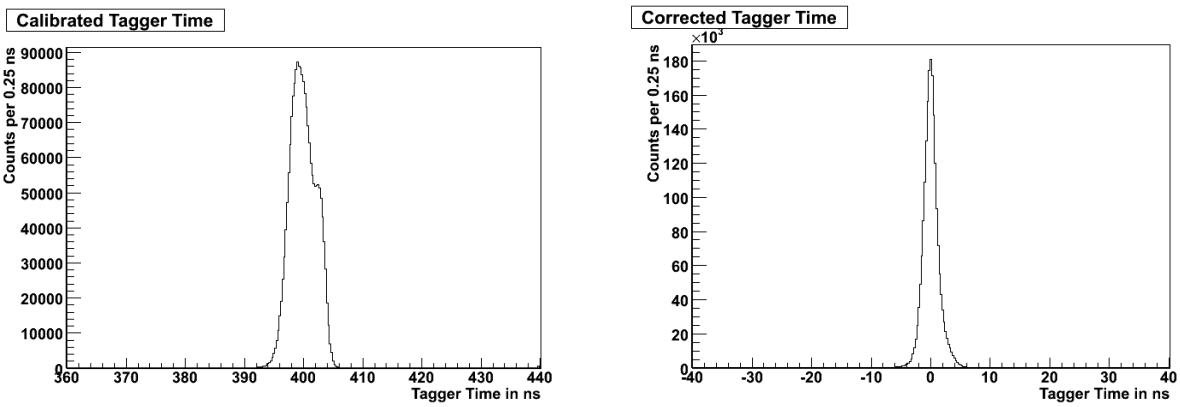

Figure 3.14: Time distribution of all tagger channels before (left) and after time walk correction (right). The overall resolution, obtained by Gaussian Fits, amounts to 2.04 ns and 1.20 ns respectively.

Both distributions were fitted with a Gaussian function. The width before correction corresponds to 2.04 ns. After correction a width of 1.20 ns is observed, which is a significant improvement in the overall time resolution.

3.3 Position Reconstruction

3.3.1 Theoretical Considerations

Typically two different approaches are chosen to reconstruct the point of impact of an incident particle into a laterally segmented electromagnetic calorimeter. Both methods are based on the calculation of the center of gravity of the induced electromagnetic shower. This is done by summing up the position of the individual detectors x_i multiplied with it's corresponding deposited energy E_i and dividing by the sum of all energies E_i.

$$x_{cg} = \frac{\sum_i w_i x_i}{\sum_i w_i} \tag{3.9}$$

$$w_i = E_i \tag{3.10}$$

As pointed out in [A+77], this algorithm delivers a systematic shift between calculated position x_{calc} and real position x. This effect is also known as S-curve and is strongest near the center and the edges of a subunit. Usually the S-curve is almost energy independent due to the fact that the Molière radius has a negligible energy dependence. Thus by fitting the S-curve and correcting x_{cg}, one can remove the bias of the algorithm

in Eq. 3.9 and linearize the position information. For electrons the 'true' position of impact x is accurately measurable, e.g. by using MWPCs[1] or a cross of scintillating organic fibers. Therefore, the S-curve can be well determined. Nevertheless, in case of photons as incident particles this is difficult to measure directly. Hence an algorithm which provides intrinsically a position with minimum systematic shift would be more appropriate. According to [A+92] this can be achieved by taking the lateral shower profile into account. Despite of a linear weighting of the position of the single detectors, a logarithmic weighting of the individual energy deposition is chosen according to the exponential falloff of the transversal profile of the electromagnetic shower. Therefore the weighting factor w_i in Eq. 3.9 is now calculated according to Eq. 3.11.

$$w_i = \begin{cases} 0 & , W_0 + \ln\left(\frac{E_i}{E_T}\right) \leq 0; \\ W_0 + \ln\left(\frac{E_i}{E_T}\right) & , \text{else}; \end{cases} \tag{3.11}$$

$$E_T = \sum_i E_i \tag{3.12}$$

The position reconstructed with this method is called x_{log}. The weighting parameter W_0 in Eq. 3.11 is roughly equivalent to the minimum fraction of deposited energy E_i to the total Energy E_T in an individual detector taken into account for position reconstruction. W_0 should be chosen high enough to deliver a Gaussian-like distribution of x_{log}, but its value should be also low enough to avoid a degradation in position resolution.

3.3.2 Position Reconstruction

The first step to perform a position reconstruction for the PROTO60 was to define a coordinate system. As Fig. 2.11 indicates, it was assumed that the projection of the crystal front faces on a plane perpendicular to the beam direction represents a grid of squares with a length of 22 mm. The origin of the coordinate system is located on the upper left corner of crystal 35. As crystal coordinates for the reconstruction algorithm the center of the squares were used. For example, the center of crystal 35 corresponds to the (x, y) coordinates (11 mm, -11 mm). The coordinates of the other crystals can be taken from in Fig. 3.15.

Center of Gravity Algorithm General conditions were requested for position reconstruction. The algorithm in Eq. 3.9 is only applied for events when the conversion before the detector can be excluded and the energy in each crystal taken into account exceeds $E_{xtl} = 1.00$ MeV. Furthermore, the multiplicity of the event is calculated

[1] **M**ulti **W**ire **P**roportional **C**hambers

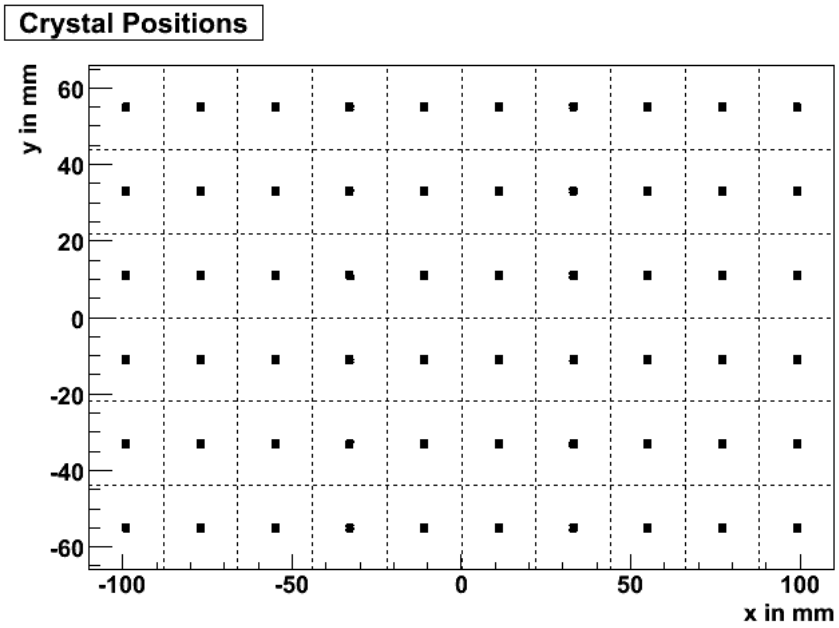

Figure 3.15: Coordinates of the crystal centers as used for the position reconstruction algorithms. Crystal 1 is placed in the upper right, crystal 60 in the lower left corner.

under the same condition and only events are selected, with a multiplicity larger than three. To avoid pile-up, it was requested that the multiplicity of the responding tagger channels is equal to one. Under this conditions x- and y-position of the incident photon are calculated. Fig. 3.16 shows the position distribution for horizontal and vertical direction for all incident energies. While the distribution of x_{cg} is symmetric, there is a slight asymmetry towards lower y_{cg}. To proof linearity, the x_{cg} distribution for the four different beam positions was used (Fig. 3.17). Following the expectations, the calculated position is biased towards the center of the crystal at 11 mm. The energy dependence of the reconstructed position and its resolution is plotted in Fig. 3.18.

Logarithmic Weighting To perform position reconstruction with the weighting, expressed in Eq. 3.11, the determination of the weighting parameter W_0 suited for the chosen energy range is crucial. Under variation of W_0 the x_{log} distributions were calculated for an matrix of 3×3, 5×5 crystals and the whole 6×10 matrix, respectively. The obtained distributions are shown for selected values of W_0 in Fig. 3.19. A value of $W_0 = 4.8$ represents a good compromise between reasonable shape and narrow width over the whole energy range. In particular in the low energy range and for a reduced matrix of 9 crystals, the central detector dominates in comparison to it's neighbors.

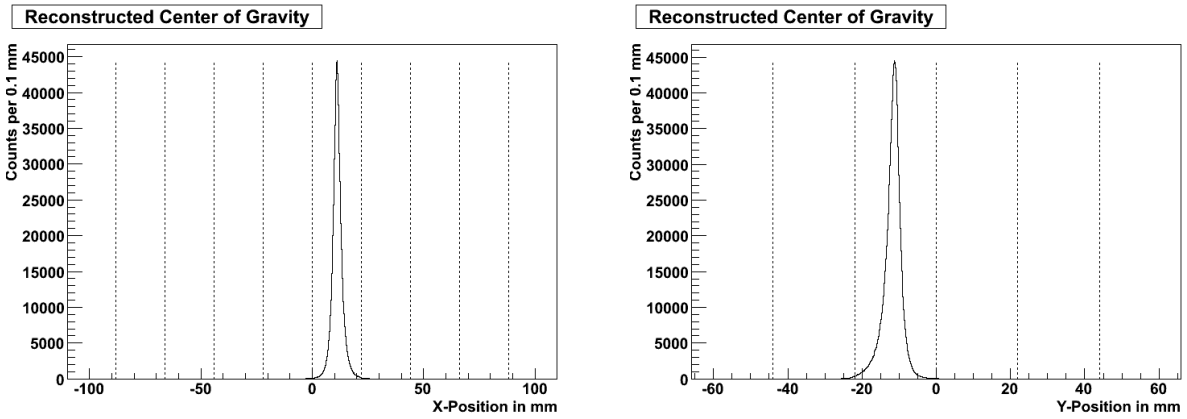

Figure 3.16: Reconstructed position distribution for the incident photons in x- (left) and y - Coordinate (right). The dashed lines represent the crystal boundaries.

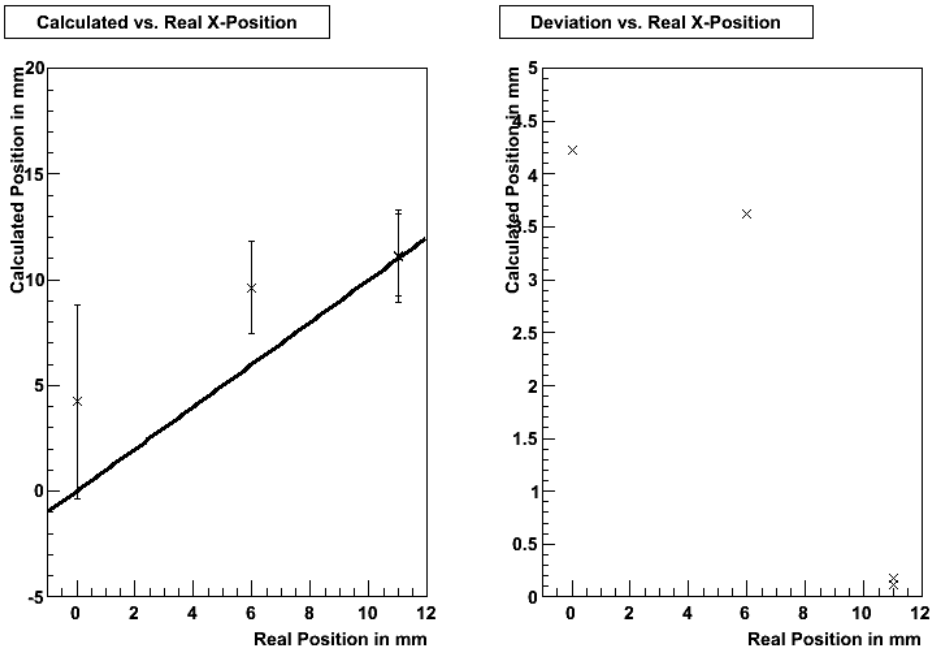

Figure 3.17: Plot of the reconstructed position x_{cg} versus the beam position (left) and the difference between them (right).

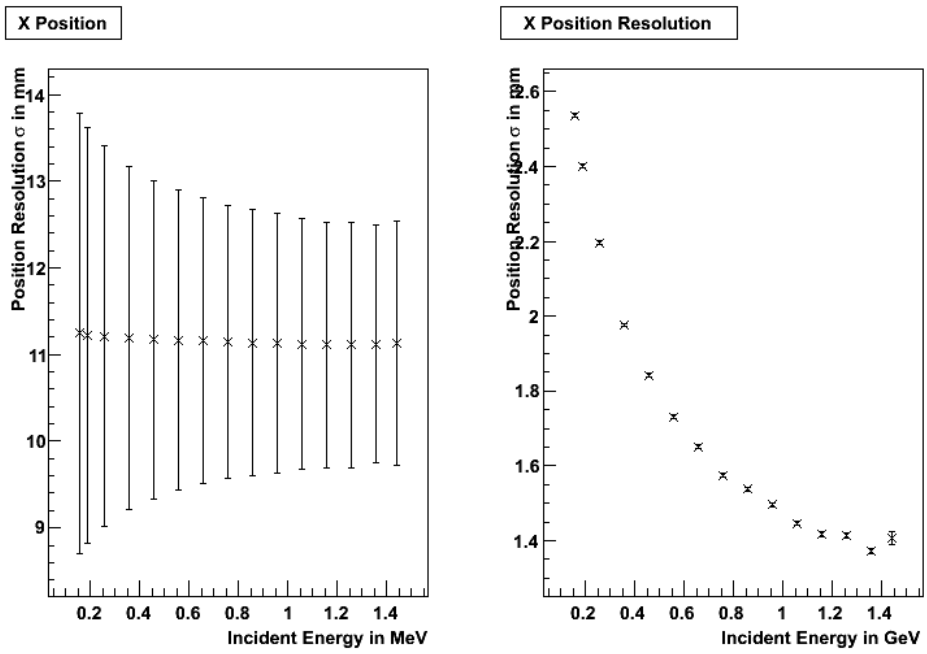

Figure 3.18: Energy dependence of x_{cg} (left) and of the corresponding resolution (right).

This leads to a spike in the distribution for lower values of W_0. After finding W_0, roughly the same analysis procedure was applied. As illustrated in Fig. 3.20, the deviations of x_{log} from the used beam position are reduced. It can also be observed, that the statistical error of x_{log} decreases with distance to the crystal center, most likely, because more energy is shared between responding modules and the dominance of the central crystal is reduced.

3.3.3 Influence of the Beamspot on the Reconstruction

As pointed out in Section 2.2, the photon beam from the tagger had a not well determined profile. As an estimate, the size of the beam was geometrically calculated according to Fig. 3.21. The used collimator had an diameter of 1.5 mm. Implying a homogeneous intensity distribution along the whole diameter, the beam spot has a maximum size of 9 mm at the front face of the PROTO60. This corresponds roughly to 40% of the Molière radius of PWO. Thus, the deduced position resolutions represent the convolution of photon beam size and intrinsic resolution. In addition, the beam width is energy dependent. Therefore, the reconstructed width of the position distribution can only be regarded as an upper limit for resolution. Both, reconstructed x_{log}- and y_{log}-distribution for all incident energies are Gaussian like and have a width

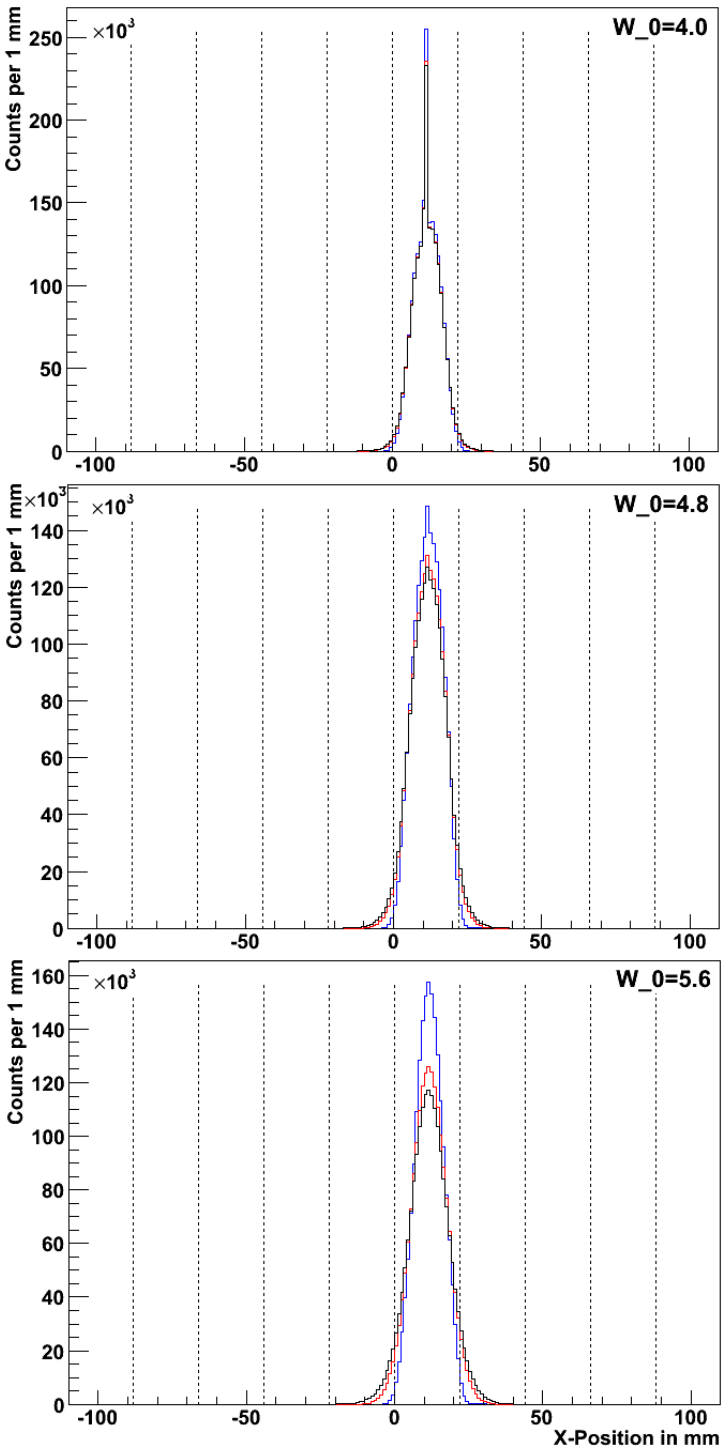

Figure 3.19: Position distributions at three different weighting parameters for a matrix of 3×3 (blue), 5×5(red), 6×10 crystals (black), respectively.

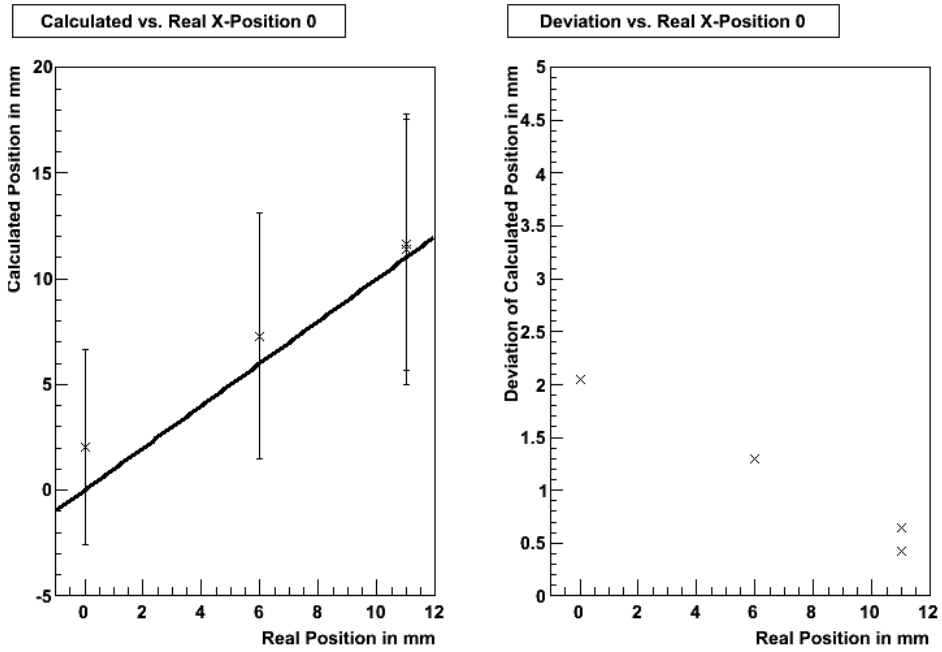

Figure 3.20: Plot of the reconstructed position x_{log} versus the beam position (left) and the difference between them (right).

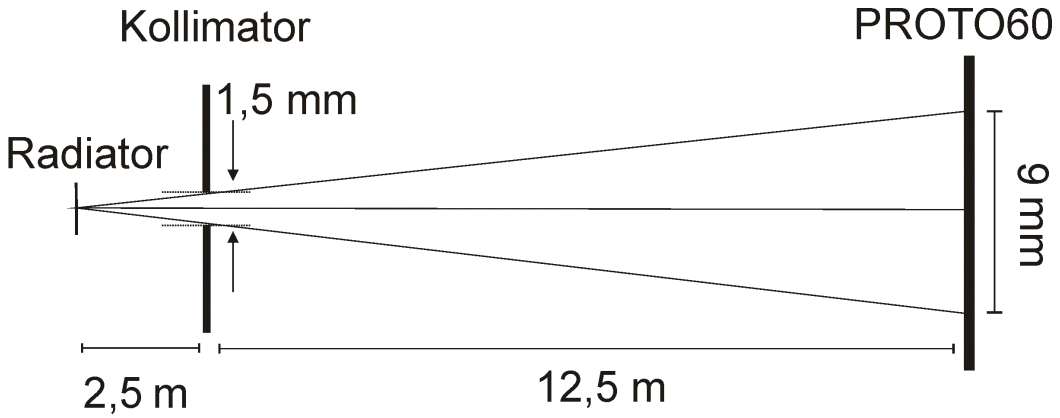

Figure 3.21: Sketch of the setup to calculate the size of the beam geometrically.

$\sigma_x \approx \sigma_y \approx 6mm$, which results in a FWHM of 14 mm. This values differ from the biased x_{cg} and y_{cg} FWHMs of 4 mm and 3 mm, respectively. The logarithmic weighting leads to more stable shapes while for the linear weighting in case of beam positions outside the center, odd shapes and strong tailings are observed, like indicated in Fig. 3.22. This is the reason why the upper limit of the resolution is determined with the weighting in Eq. 3.11.

3.3.4 Achieved Position Resolutions

The resolutions of the x_{log}-distributions for different incident energies were fitted with a Gaussian function. The mean positions, indicating the width σ_x as error, are plotted versus the incident energy in Fig. 3.23. Whereas the reconstructed mean position is not varying with the incident energy, the width σ_x indeed does (Fig. 3.23, right). The results are parametrized by Eq. 3.13, which leads to a position resolution of $\sigma_x = 4.3$ mm at 1 GeV.

$$\sigma_x = \sqrt{(3.45 \text{ mm})^2 + \left(\frac{2.62 \text{ mm}}{\sqrt{E/\text{GeV}}}\right)^2} \tag{3.13}$$

For y-direction, the picture is roughly the same. An overview over the position resolution restricted to different sub-arrays provides Table 3.1. While for a matrix of 60 and

Array	σ_x	σ_y
3×3	3.7 mm	3.7 mm
5×5	4.3 mm	4.2 mm
6×10	4.3 mm	4.2 mm

Table 3.1: Position resolution at 1 GeV for different crystal arrays with beam in central position.

25 crystals we end up with the same resolution at high energies, there is a difference up to 1 mm at the lowest energy of 158 MeV. Nevertheless the obtained width σ_x for an array of only 9 crystals is lower over the whole energy range and the distributions are less smooth. This is understandable, because the energy deposit in the second ring is not taken into account and therefore one expects some slight bias to the center as for the x_{cg}.

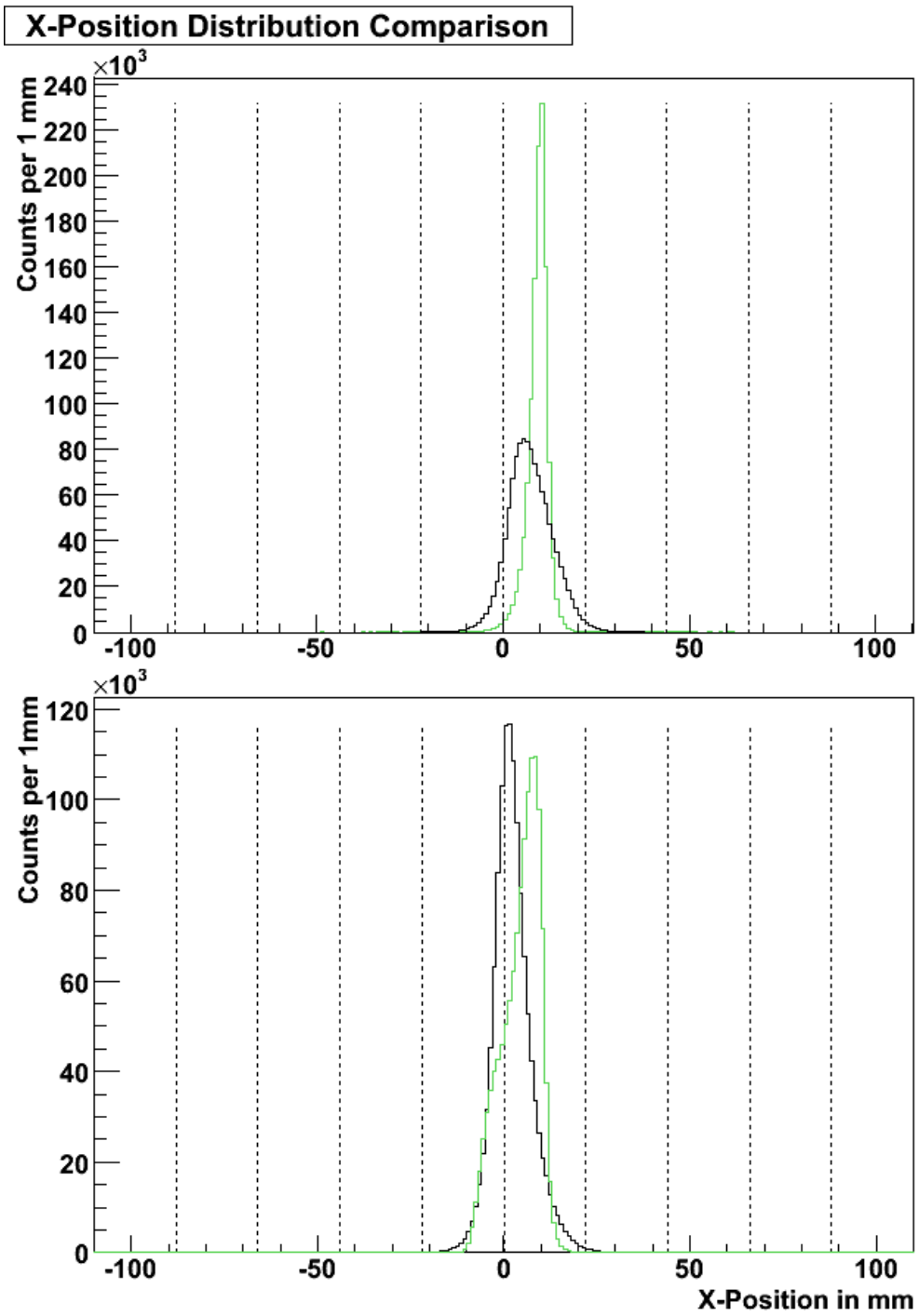

Figure 3.22: Comparison of x_{cg}- (green) and x_{log}- distribution for the beam position corresponding to $x = 6$ mm (above) and $x = 0$ mm (below).

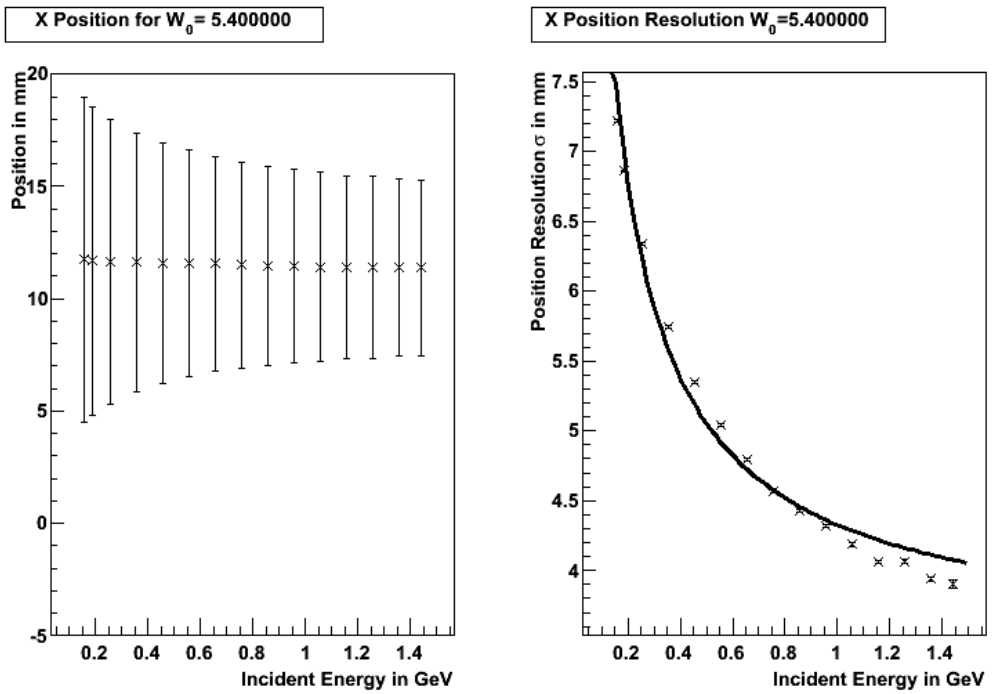

Figure 3.23: Energy dependence of x_{log} (left) and of the corresponding resolution (right) for the whole crystal array.

Chapter 4

Comparison to Simulations on the Basis of PandaROOT

4.1 The PandaROOT Software Package

The offline simulation framework for $\overline{\text{P}}$ANDA is called PandaROOT. It is developed within the FairROOT project which has the aim to provide a common computing structure for all experiments at the FAIR facility. PandaROOT is based on the object oriented analysis software package ROOT, developed at CERN[1]. The framework can be divided into three main parts, as illustrated in Fig. 4.1. Several event generators

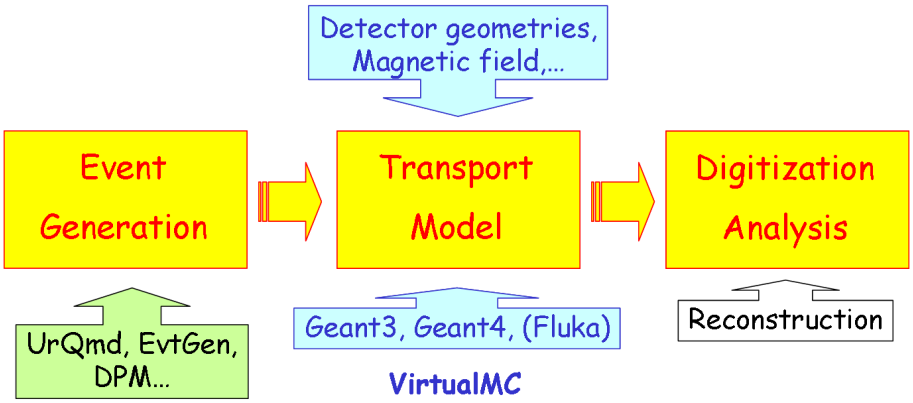

Figure 4.1: Scheme of the PandaROOT framework's structure [Spa08].

provide the input parameters of either Geant3 or Geant4. These are transport models based on Monte Carlo calculations to simulate interactions of particles with the detector (see [A+03]). The data produced by Geant3/4 are stored in a tree format,

[1] **C**onseil **E**uropéen pour la **R**echerche **N**ucléaire

which is a native ROOT structure. Hence it is natural to perform data modifications, e.g. like to mimic digitisation effects and further analysis with ROOT. One major advantage of using PandaROOT instead of the bare Geant software package is the already implemented detector geometry of the whole $\overline{\text{P}}$ANDA Detector and its individual components in their current development status.

4.2 Assumptions

As mentioned in Section 2.1.1, the PROTO60 represents a part of a barrel EMC slice. Therefore, it was natural to select the corresponding section of the setup implemented in PandaROOT, rather than to define a completely new PROTO60 geometry. The procedure was to reduce the implemented barrel geometry to a ring covering nearly the same angle θ with respect to the beam direction as the prototype. The full azimuthal angle ϕ was still defined by the geometry, but only the first slice was read out by the software. One main difference to the real PROTO60 geometry is the fact, that two crystal rows are of geometry type 5, whereas in the prototype exclusively type 6 was used (compare Fig. 4.2). Another difference is the missing dead material in front of the barrel EMC subunit and between the crystals. Two steps of the simulation

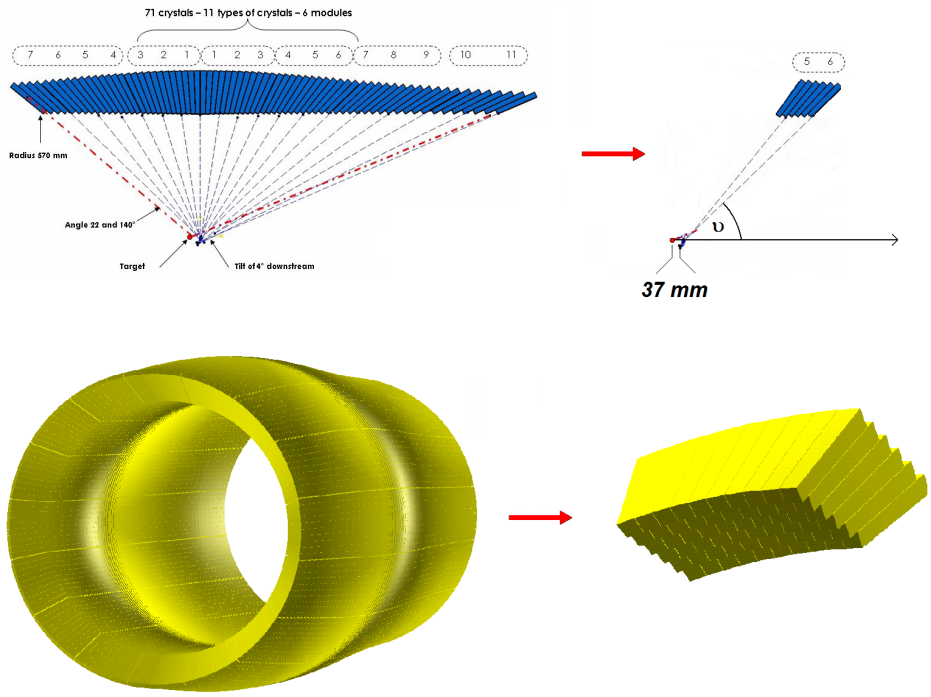

Figure 4.2: Schematic view of the selected simulation geometry.

were performed. The Monte Carlo simulation applied the default Geant4 settings of PandaROOT without further fine-tuning. From the original output data of the applied Geant4 transport model, represented by Monte-Carlo tracks of interacting particles in the detector, the deposited energy in the subdetectors is determined. These detector hits, originally stored in a tree structure, were converted in a way they could be read out by the same code applied for the analysis of the test run. This enables an easy comparison between simulation and experiment.

Single photons were impinging on the center of crystal 5 in the 22^{nd} row of module 1, which corresponds to crystal 35 of the PROTO60. Four photon energies were selected, representing the tagger channels 16, 10, 5 and 1 as given in Table 2.1. For each energy, two different start distributions were generated. The first version was a pointlike photon beam pointing at $\vartheta = 47.5°$ and $\varphi = 88.4°$, respectively. The other one was a cone with opening angle of 0.6° with homogeneous intensity distribution as shown in Fig. 4.3, to reproduce the 9 mm beamspot on the front of the detector surface. The emission point of the photons was shifted 3.7 cm downstream the beam,

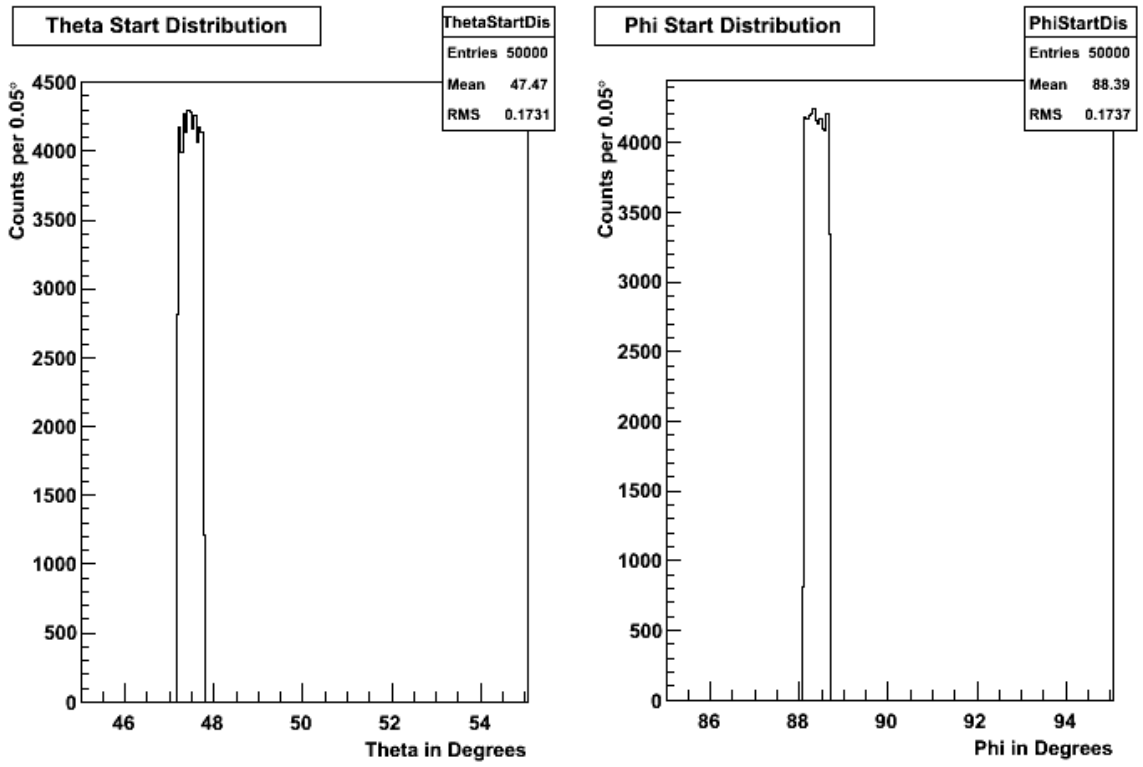

Figure 4.3: Start distribution of the incident photons, representing a cone with opening angle 0.6°. Over a distance of 83 cm this corresponds to a 9 mm beamspot

in order to achieve a perpendicular impact (compare Fig. 4.2). The shifting of the

vertex in φ direction was neglected.

4.3 First Results

4.3.1 Energy Resolution

The pure information about the energy deposition in the individual crystals, called hit energy in the simulations was analysed with a similar code as for the real data of the beamtest. The resulting line shapes for different subarrays are shown in Fig. 4.5 and Fig. 4.4 for the simulated energies. In comparison to Fig. 3.2, the Fig. 4.6 shows

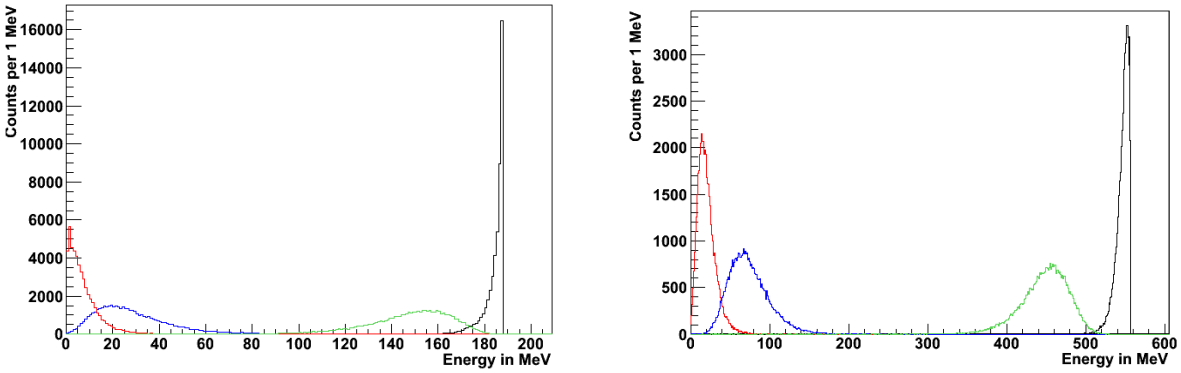

Figure 4.4: Line shape of energy sum (black), central crystal (green), first ring (blue) and second ring (red) at an incident photon energy of 188 MeV (left) and 557 MeV (right), respectively.

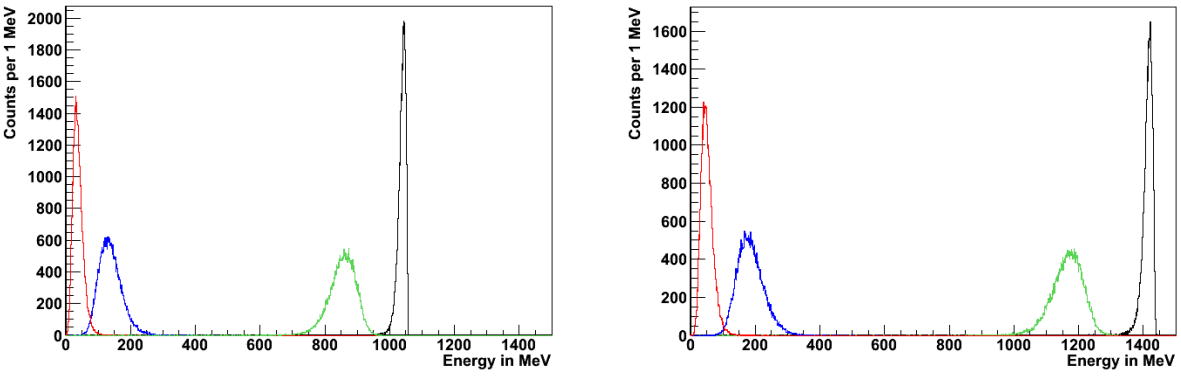

Figure 4.5: Line shape of energy sum (black), central crystal (green), first ring (blue) and second ring (red) at an incident photon energy of 1058 MeV (left) and 1441 MeV (right), respectively.

the energy sum for an energy of 1058 MeV deduced from simulation. A fit with the

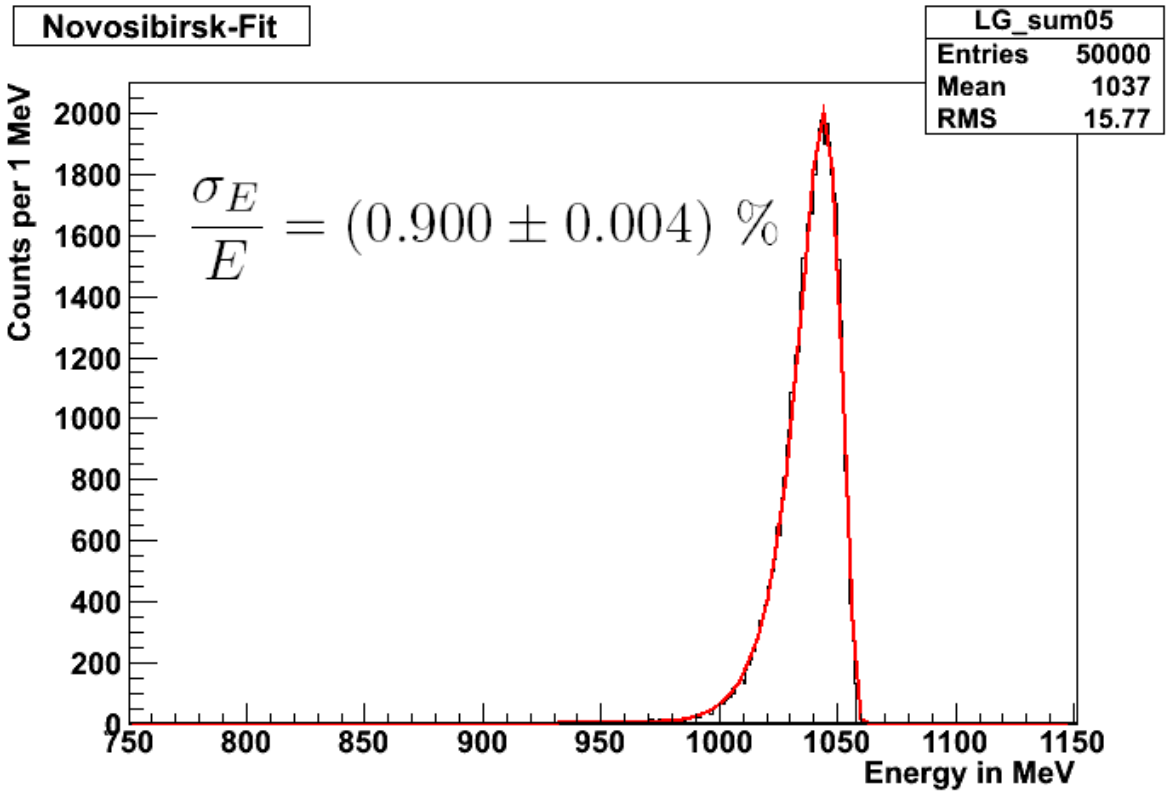

Figure 4.6: Novosibirsk fit of the energy sum for an incident energy of 1058 MeV.

Novosibirsk function gives a relative energy resolution of $\frac{\sigma_E}{E} = 0.9\%$ which is a factor 2.7 better than in the experiment. An overview of the Energy resolution obtained for all simulated energies, is given in Tab. 4.1.

4.3.2 Position Resolution

The simulated data was also analysed with regard to position reconstruction. A comparison of simulation and experimental data regarding the distributions for both directions and algorithms at an incident energy of 1058 MeV is displayed in Fig. 4.7 and Fig. 4.8. An overview of the obtained results for x- and y- distributions is given in Tab. 4.2 and Tab. 4.3, respectively. Both algorithms with linear and logarithmic weighting were used.

Contrary to the expectations, the difference between the reconstructed positions for pointlike and cone shaped beam is only small. Nevertheless, the reconstructed position and width agree within a deviation of 0.5 mm with the experiment results except for

Simulation			
Energy in MeV	E **in MeV**	σ_E **in MeV**	$\frac{\sigma_E}{E}$ **in %**
188	187	1.0	0.52
557	551.8	4.7	0.84
1058	1044.55	9.35	0.90
1441	1421.18	11.64	0.82

Table 4.1: Overview of the energy resolution deduced from simulation at different incident photon energies. The photon beam had an opening angle of $\vartheta = 0.6°$.

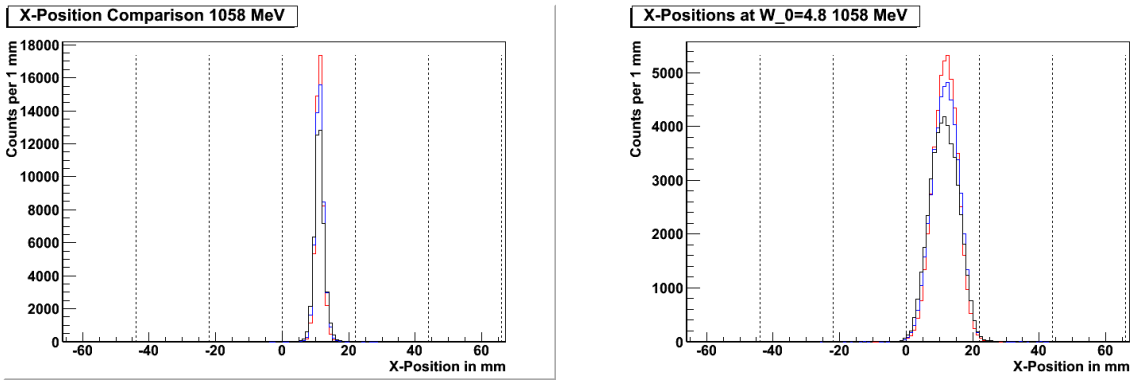

Figure 4.7: Distribution of x_{cg} (left) and x_{log} (right) for simulation with (blue) and without (red) beam opening angle in comparison to data. The black curve has slightly less statistics.

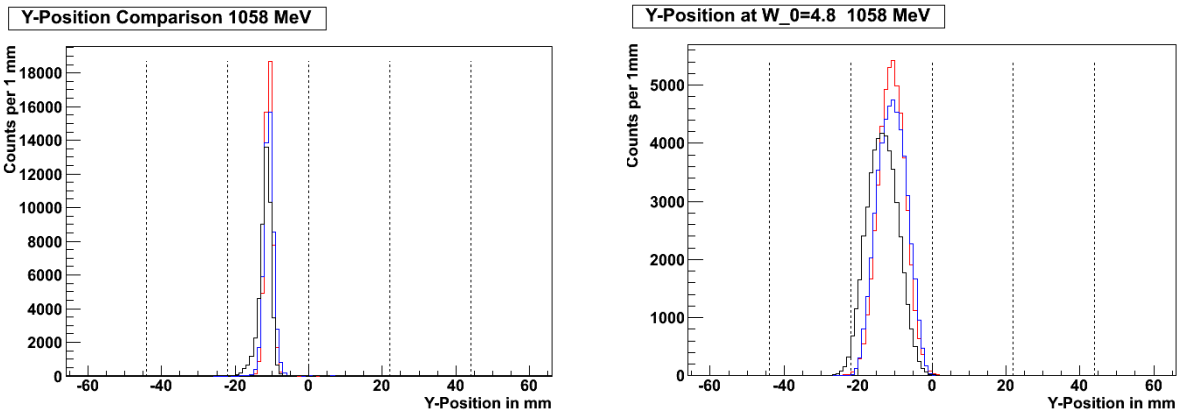

Figure 4.8: Distribution of y_{cg} (left) and y_{log} (right) for simulation with (blue) and without (red) beam opening angle in comparison to data. The black curve has slightly less statistics.

Simulation				
Energy in MeV	**Pencil Beam**		**Opening Angle**	
	x_{cg} in mm	σ_x in mm	x_{cg} in mm	σ_x in mm
1441	11.2	1.0	11.2	1.2
1058	11.2	1.1	11.2	1.3
557	11.3	1.5	11.3	1.6
188	11.3	2.3	11.4	2.5
	x_{log} in mm	σ_x in mm	x_{log} in mm	σ_x in mm
1441	11.7	3.2	11.7	3.6
1058	11.8	3.7	11.8	4.0
557	11.9	4.8	11.9	5.0
188	12.0	7.2	12.0	7.2
Experiment				
Energy in MeV	x_{cg} in mm	σ_x in mm	x_{log} in mm	σ_x in mm
1441	11.1	1.4	11.4	3.9
1058	11.1	1.4	11.4	4.2
557	11.2	1.7	11.6	5.0
188	11.2	2.4	11.7	7.2

Table 4.2: Overview of x-position and resolution for simulation and experiment at different incident photon energies.

Simulation				
Energy in MeV	**Pencil Beam**		**Opening Angle**	
	y_{cg} in mm	σ_y in mm	y_{cg} in mm	σ_y in mm
1441	-10.8	0.9	-10.8	1.2
1058	-10.8	1.0	-10.8	1.3
557	-10.7	1.4	-10.8	1.6
188	-10.7	2.1	-9.2	2.5
	y_{log} in mm	σ_x in mm	y_{log} in mm	σ_y in mm
1441	-10.9	3.1	-10.9	3.8
1058	-10.8	3.6	-10.8	4.1
557	-10.6	4.6	-10.6	5.0
188	-10.1	6.5	-9.2	6.8
Experiment				
Energy in MeV	y_{cg} in mm	σ_y in mm	y_{log} in mm	σ_y in mm
1441	-11.7	1.3	-13.4	3.8
1058	-11.7	1.4	-13.3	4.1
557	-11.6	1.7	-13.1	4.9
188	-11.5	2.3	-12.5	6.4

Table 4.3: Overview of y-position and resolution for simulation and experiment at different incident photon energies.

the reconstructed y-position. Both algorithms show a systematic shift which reaches up to -1 mm in the case of y_{cg} and -3 mm in the case of y_{log}, respectively. Such a shift in absolute position is understandable, because the beam position during the test run was adjusted with limited accuracy and the described geometrical approximations in reconstruction have been made. That the y-position shifts to higher values at lower incident energies is most likely caused by the staggering of the crystals. The depth of maximum energy deposition of an electromagnetic shower in lead tungstate, calculated according to Tab. 1.2, amounts to $z_{max}^{188\ \mathrm{MeV}} = 2.3$ cm for 188 MeV photons and to $z_{max}^{1441\ \mathrm{MeV}} = 4.1$ cm for 1441 MeV photons, respectively. For low energy photons the shower maximum is located within the first few centimeter, where the crystals are staggered. This geometrical fact can cause an asymmetry in the transversal energy distribution. In case of PROTO60, one would expect a shift with decreasing energy to higher values of the reconstructed y-coordinate.

Chapter 5

Discussion and Outlook

First analysis results of the PROTO60 beamtest performed in February 2009 are worked out in [Mor09]. That thesis describes in detail the procedure of the energy calibration and deduces the energy response function of the PROTO60. Eq. 5.1 represents the parametrisation of the energy resolution and meets the requirements of the TDR, shown in Tab. 1.3.

$$\frac{\sigma_E}{E} = 0.61\% \oplus \frac{1.83\%}{\sqrt{E}} \tag{5.1}$$

The obtained result is well below the specification limits and shows that an excellent energy resolution is achievable also with a readout inferior to the one proposed for the EMC. The scintillation light will be finally collected by two LAAPDs and converted into an electronical signal by an optimised preamplifier ASIC[1]. In continuation, this thesis focuses on the time and position information of the PROTO60 and a first comparison with standard simulations on the basis of the Geant4 transport model included in the PandaROOT framework. The experimental data of PROTO60 are used for a first check of the start parameters for this $\overline{\text{P}}$ANDA-specific simulation package.

5.1 Achieved Results in Comparison to the TDR and General Expectations

As expected, a position dependence of the energy resolution was observed (compare Fig. 3.5). A final quantitative statement is difficult, since the influence of the beam profile is not well known. Nevertheless, a clear trend of degradation in resolution occurs for beam positions shifted from the center of a crystal. In addition, the magnitude of the change in resolution depends on the incident energy. Therefore, a more detailed

[1] **A**pplication **S**pecific **I**ntegrated **C**ircuit

and quantitative study appears necessary to guarantee an optimized particle reconstruction in future experiments. Experience of the CMS-Collaboration[2] described in [DJ06] shows that an accurate measurement of the dependencies, e. g. with an electron beam impinging on different positions, can be used to develop a correction algorithm.

Without aiming for an optimisation, a first experimental proof for the achievable time resolution was deduced. An overall resolution of $\sigma_t = 1.2$ ns was obtained, which is better than the limit referred in the TDR [PAN08], which requires for the timing of an individual unit 3 ns. For previous smaller test arrays of lead tungstate read out via photomultipliers, superior resolutions were obtained documenting the excellent timing performance of PWO [M$^+$98]. With a matrix of 5×5 crystals at a temperature of $T = 8°$C a time resolution of 417 ps and 240 ps was measured at photon energies of 59 and 790 MeV, respectively. The achieved resolution for the PROTO60 is limited by the APD readout, due to longer rise times compared to photomultipliers. Nevertheless, the parametrisation in Eq. 3.6 shows, that a sub-nanosecond resolution is achieved for deposited energies above 0.6 GeV. At 1 GeV deposited energy, the time resolution amounts to 680 ps. Recent measurements reading out the prototype detectors with Sampling-ADC show that resolutions of 500 ps to 600 ps can be obtained even for energies above 150 MeV [Kav]. The achievable resolution does not allow to perform time of flight measurements, but provides good correlations to other detector parts for particle ID or to reduce background.

Position reconstruction for incident photons was performed with a state-of-the-art procedure. By applying the non-linear weighting of Eq. 3.11 together with a center of gravity algorithm (Eq. 3.9), a linear response is achieved without applying further corrections. Due to the uncertainty of the influence of the intensity distribution of the photon beam profile, the obtained resolutions can be regarded as an upper limit. The reconstructed position in x-direction is stable and variations with incoming energy are negligible, but for vertical direction a significant deviation at decreasing incident energy is observed. If the reconstruction is restricted to an array of 3×3, distributions are less stable but also the reconstructed width becomes smaller. The restriction to a 5×5 array shows no significant difference to calculations taking the whole detector into account since there is no significant energy spread due to the lateral shape of the shower in the investigated energy regime. Thus, for later application in the barrel EMC, cluster arrays of 25 crystals provide sufficient position information. The energy dependence of the resolution in both x- and y- direction is roughly parametrised by

$$\sigma_x \approx \sigma_y = 3.4 \text{ mm} \oplus \frac{2.6 \text{ mm}}{\sqrt{E/\text{GeV}}}. \tag{5.2}$$

[2] **C**ompact **M**uon **S**olenoid Experiment

This upper limit in position resolution of 4.3 mm at 1 GeV represents roughly $\frac{2}{10}$ of a crystal front face. Experiments with lead tungstate test arrays at room temperature and rectangular crystal geometries have also been made by other groups. For incident electrons impinging an 5×5 array, Batarin et al. [B$^+$03] obtain a spatial resolution of $\sigma_x = 0.17 \text{ mm} \oplus \frac{2.77 \text{ mm}}{\sqrt{E/\text{GeV}}}$, while Shimizu et al. [SSH$^+$00] measure $\sigma_x = 0.4 \text{ mm} \oplus \frac{2.6 \text{ mm}}{\sqrt{E/\text{GeV}}}$ for a 3×3 array. Both groups applied a linear weighting and corrected for non-linearities afterwards.

5.2 Comparison to Simulations and Unsolved Issues

Simulations with the default settings of PandaROOT for the Geant4 input parameters were performed, intending to investigate if the delivered transversal shower shape is in accordance with experiment. A subunit of the implemented barrel EMC geometry, representing PROTO60, was chosen and single photons with fixed energy were impinging in the center of a crystal. The information on the pure deposited energy in the detector modules was used to determine the ideal detector energy response. A comparison of experimental and simulation result is plotted in Fig. 5.1. Due to the setting of a low energy threshold, almost no energy is lost in a geometry which contains no dead material. At lower energy the whole shower is contained in the detector volume. However, for higher energies shower leakages caused by shower fluctuations lead to a slight degradation in resolution. If the threshold is increased to cut off low energy depositions in neighboring crystals, resolution becomes significantly worse at lower energies and the shape of the energy dependence is closer to experimental results.

As a criteria for the transversal shape of the electromagnetic shower, the ratios of the mean deposited energy in central crystal, first and second ring and the rest of the detector to the total energy sum $R_n = \frac{E_n}{E_T}$ were defined. The E_n and E_T were determined by fitting the peaks in Fig. 4.4 and Fig. 4.5 with a Novosibirsk function.

Like Tab. 5.1 indicates, the simulation differs only slightly from experiment. The shower shape seems to be well reproduced, although no dead material like the carbon sheets between the crystals is implemented. However, the simulated data is not suited to reproduce the line shapes. This has to be performed in detail by more sophisticated simulations, including photon statistics, electronic noise and contributions due to the final digitisation.

Since the lateral shower distribution agrees with the experiment, one expects that position reconstruction is in accordance as well. Indeed, resolution and peak positions are reproduced very well within slight deviations up to half a millimeter. For simulated pencil beam and cone beam, no big difference is observed (compare Fig. 4.7 and

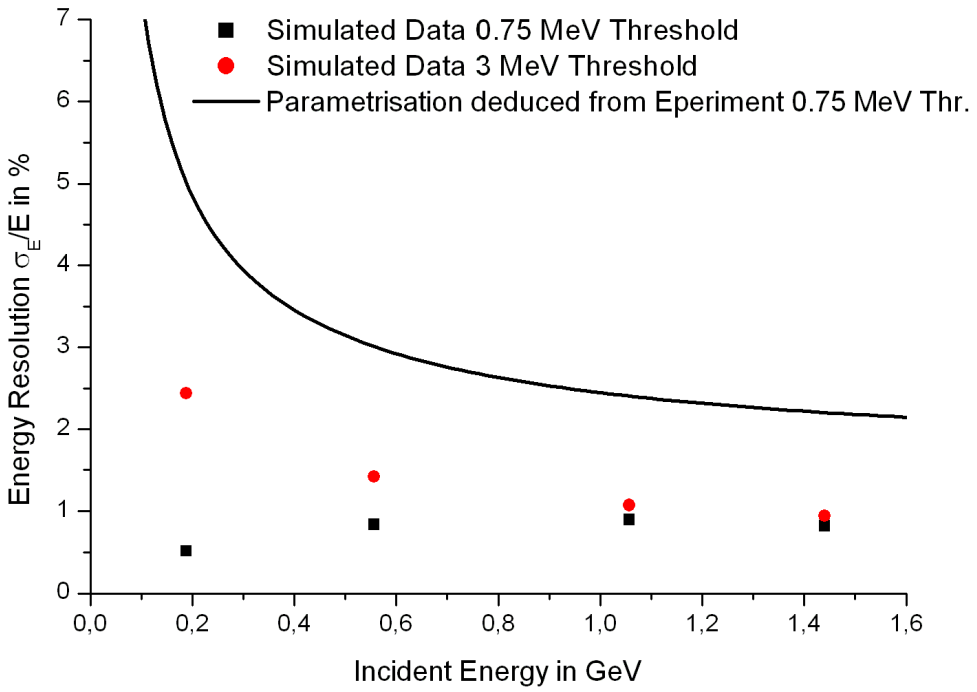

Figure 5.1: Comparison of the deduced energy resolution parametrisation for experiment (line) and the ideal resolution obtained in the simulation (dots) for a beam with opening angle $\vartheta = 0.6°$.

	Energy in MeV	**Ratios in %**			
		R_{Center}	R_{First}	R_{Second}	R_{Rest}
Experiment	1441	81.35	13.88	3.16	0.31
	1058	81.65	13.67	2.87	0.30
	557	82.03	13.10	2.87	0.30
	188	82.36	11.25	1.27	0.49
Simulation	1441	82.79	12.35	3.13	0.46
	1058	82.76	12.20	3.03	0.42
	557	82.85	11.68	2.67	0.37
	188	82.94	10.43	0.89	0.64

Table 5.1: Ratios of the deposited energies in different rings for simulation and experiment.

4.8). This is understandable if one assumes that the reconstructed position distribution is represented by a convolution of intrinsic resolution and beam shape. Another remarkable effect is, that for experiment and even more pronounced for simulation, the reconstructed y-distribution shifts strongly to higher reconstructed positions at low energies. This effect is most likely caused by the staggering of crystals within the detector array (shown e.g. in Fig. 4.2). In the experiment this effect will be a source for inaccuracies in position determination, especially at low energies and a development of correction procedures should be considered.

5.3 Improvement of Calibration Methods

5.3.1 Vertically Mounted PROTO60

The calibration method described in Section 2.3, was mostly appropriate for lower energies. In order to improve and extend calibration to higher energies, the mechanical arrangement of the PROTO60 was modified to rotate the prototype by 90°. In this position the front faces of the crystals are pointing vertically (shown in Fig. 5.2). This has the advantage that cosmic rays pass the full length of one crystal, which is identical for each crystal. In that case, minimum ionizing muons have an average energy deposition in one subunit of 204 MeV, which is a factor 8.5 higher than before. The maximum deviation of the deposited energy due to different passlength is of the order of 1%. First measurements of cosmic rays were performed with either an external cosmic trigger or a self trigger of each crystal at a high energy threshold (compare Fig. 5.3). The external cosmic trigger was represented by the coincidence of two plastic scintillator paddles. One of these was not working properly, resulting in a long time of measurement. Nevertheless, by using the self trigger it was determined that one week of measurement is sufficient to provide enough statistics to perform a proper calibration.

5.3.2 Cross of Inorganic Fibers for Beam Monitoring

Recent developments made the production of thin fibers of inorganic scintillators, e.g. LYSO[3], possible. The short radiation length, due to the high atomic number Z, of inorganic scintillators in comparison to organic material will allow in addition an efficient response to high energetic photons. This provides the opportunity to construct a position sensitive detector. Such a detector will provide automatically a spatial resolution given by the fiber diameter. Thus, it could serve to measure intensity

[3] Cerium doped **L**utetium**Y**ttrium **O**rtho**s**ilicate

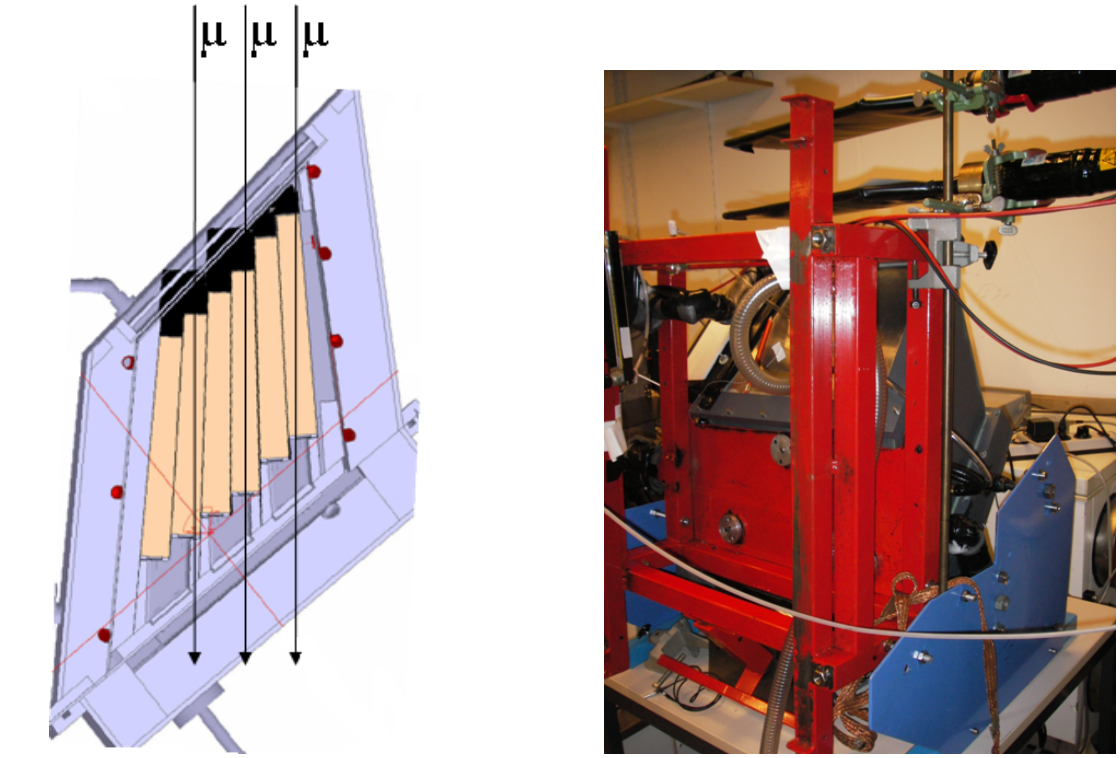

Figure 5.2: PROTO60 mounted in vertical direction. Cosmic muons are now able to pass the full length of a crystal.

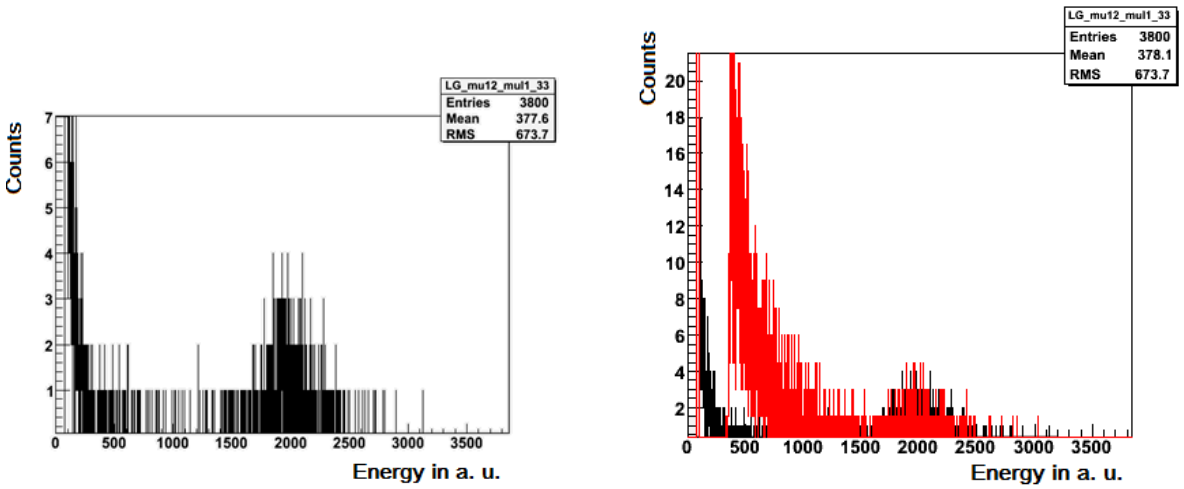

Figure 5.3: Cosmic spectrum of the vertically mounted PROTO60 recorded with an external trigger (left) under the condition, that only one crystal responded and had an energy deposition above $12\sigma_{Noise}$. Comparison with a spectrum recorded with self triggered modules (right), requiring a multiplicity of one.

distributions of electron and photon beams as well. Furthermore an inorganic fiber cross could provide a reliable and accurate position reference for future beam tests of EMC prototypes, which would help to consolidate the results obtained in this thesis and improve the knowledge about the detector response.

List of Figures

1.1 Artistic view of the present GSI and the planned future facility FAIR . 3
1.2 Accessible mass range with respect to the required antiproton momentum 5
1.3 Lattice-QCD predictions for the charmonium, the glueball and the spin-exotic $c\bar{c}$-glue hybrids spectrum in quenched lattice OCD. 5
1.4 Artists view of the Hypernuclear Chart. 7
1.5 Two possible decays of a hybrid state called X 8
1.6 Schematic view of the development of an electromagnetic shower 9
1.7 Longitudinal and transversal shower distribution in $CsI(Tl)$ 11
1.8 Schematic cross section of the $\overline{\mathrm{P}}$ANDA target spectrometer 14
1.9 Beam momentum dependence of invariant mass resolutions and hit rate in the barrel EMC 15

2.1 Schematic view of the EMC region represented by the PROTO60 . . . 18
2.2 PWO-II crystals produced for the PANDA detector. 18
2.3 Staggered PROTO60 crystals wrapped with reflector material and equipped with LAAPDs. 18
2.4 Carbon alveoles manufactured for PANDA during a test of mechanical stability. 19
2.5 Exploded view of one subunit of the future barrel EMC. 19
2.6 Photo of the PROTO60 seen from the rear side 20
2.7 PROTO60 with all backplanes mounted. 20
2.8 Layout of the DAQ electronics of the PROTO60 21
2.9 Sequence of the three MAMI racetrack-microtrons to accelerate electrons up to an energy of 855 MeV. 23
2.10 Schematic view of the doublesided harmonic microtron at MAMI . . . 23
2.11 Schematic front view of the PROTO60 with beam coordinates 25
2.12 Side view of the PROTO60 during the test run in February 2009 25
2.13 Schematic view of the setup with the tagger and the PROTO60 26
2.14 Example of minimum ionizing peak, caused by cosmic muons, fitted with a Landau function [Mor09]. 27
2.15 Spectrum of the pedestal, fitted with a Gaussian function [Mor09]. . . . 27
2.16 Schematic drawing of the pass track of comsmic muons through one column of the PROTO60. 28

3.1 Line shapes of different arrays . . . 30
3.2 Novosibirsk fit of the energy sum peak . . . 31
3.3 Linearity of the energy response . . . 31
3.4 Energy dependence of the relative energy resolution . . . 32
3.5 Position dependence of energy resolution . . . 33
3.6 Diagram of the already calibrated tagger time vs the deposited energy in the central crystal . . . 35
3.7 Time walk spectrum of two adjacent tagger channels . . . 36
3.8 Prompt time signal of the testpulser digitized by the TDC with and without a delay . . . 36
3.9 Mean value of the projected energy slices fitted with a Gaussian function. 37
3.10 Fit of calibrated tagger time vs. the energy deposited in crystal 35 . . . 38
3.11 Corrected tagger time . . . 38
3.12 Overview of the time spectra of the 15 tagger channels . . . 39
3.13 Energy dependence of the time resolution . . . 40
3.14 Time distribution of all tagger channels before and after time walk correction . . . 41
3.15 Coordinates of the crystal centers as used for the position reconstruction algorithms . . . 43
3.16 Reconstructed position distribution for the incident photons in x- and y - Coordinate . . . 44
3.17 Plot of the reconstructed position x_{cg} versus the beam position and the difference between them . . . 44
3.18 Energy dependence of x_{cg} and the corresponding resolution . . . 45
3.19 Position distributions at three different weighting parameters for different crystal matrices . . . 46
3.20 Plot of the reconstructed position x_{log} versus the beam position and the difference between them . . . 47
3.21 Sketch of the setup to calculate the size of the beam geometrically. . . . 47
3.22 Comparison of x_{cg}- (green) and x_{log}- distribution for the beam position corresponding to $x = 6$ mm (above) and $x = 0$ mm (below). . . . 49
3.23 Energy dependence of x_{log} and of the corresponding resolution for the whole crystal array . . . 50

4.1 Scheme of the PandaROOT framework's structure [Spa08]. . . . 51
4.2 Schematic view of the selected simulation geometry. . . . 52
4.3 Start distribution of the incident photons . . . 53
4.4 Line shape of energy sum, central crystal, first ring and second ring at an incident photon energy of 188 MeV and 557 MeV . . . 54
4.5 Line shape of energy sum, central crystal, first ring and second ring at an incident photon energy of 1058 MeV and 1441 MeV . . . 54
4.6 Novosibirsk fit of the energy sum for an incident energy of 1058 MeV. . 55

4.7 Distribution of x_{cg} and x_{log} for simulation with and without beam opening angle in comparison to data 56
4.8 Distribution of y_{cg} and y_{log} for simulation with and without beam opening angle in comparison to data 56

5.1 Comparison of the deduced energy resolution parametrisation for experiment and simulation 64
5.2 PROTO60 mounted in vertical direction 66
5.3 Cosmic spectra for vertical mounting 66

List of Tables

1.1 Cross section dependence on energy and atomic number for different interactions of photons with matter. 8
1.2 Determination of the longitudinal distribution of an electromagnetic shower caused by photons or electrons 10
1.3 Several selected requirements for the $\overline{\mathrm{P}}$ANDA EMC. 15

2.1 Overview of the selected tagger channels and the corresponding photon energy E_γ. 26

3.1 Position resolution at 1 GeV for different crystal arrays with beam in central position. 48

4.1 Overview of the energy resolution deduced from simulation at different incident photon energies 56
4.2 Overview of x-position and resolution for simulation and experiment at different incident photon energies. 57
4.3 Overview of y-position and resolution for simulation and experiment at different incident photon energies. 58

5.1 Ratios of the deposited energies in different rings for simulation and experiment. 64

Bibliography

[A+77] G.A. Akopdjanov et al. Determination of photon coordinates in a hodoscope cherenkov spectrometer. *Nuclear Instruments and Methods*, 140(3):441 – 445, 1977.

[A+92] T. C. Awes et al. A simple method of shower localization and identification in laterally segmented calorimeters. *Nuclear Instruments and Methods in Physics Research Section A: Accelerators, Spectrometers, Detectors and Associated Equipment*, 311(1-2):130 – 138, 1992.

[A+03] S. Agostinelli et al. G4–a simulation toolkit. *Nuclear Instruments and Methods in Physics Research Section A: Accelerators, Spectrometers, Detectors and Associated Equipment*, 506(3):250 – 303, 2003.

[Ams08] Amsler, C. et al. (Particle Data Group). *Physics Letters B*, 667(1), 2008.

[B+03] V. A. Batarin et al. Precision measurement of energy and position resolutions of the BTeV electromagnetic calorimeter prototype. *Nuclear Instruments and Methods in Physics Research Section A: Accelerators, Spectrometers, Detectors and Associated Equipment*, 510(3):248 – 261, 2003.

[DJ06] J. Descamps and P. Jarry. Periodic position dependence of the energy measured in the CMS electromagnetic calorimeter. 2006. CERN-CMS-NOTE-2006-045.

[K+85] H. Koch et al. Proposal: meson spectroscopy at LEAR with a 4 π neutral and charged detector. Technical Report CERN-PSCC-85-56. PSCC-P-90, CERN, Geneva, 1985.

[Kav] Kavatsyuk, Myroslav (*KVI*). private communications.

[LR09] Claude Leroy and Pier Giorgio Rancoita. *Principles of radiation interaction in matter and detection; 2nd ed.* World Scientific, Singapore, 2009.

[M+98] K. Mengel et al. Detection of monochromatic photons between 50-MeV and 790- MeV with a PbWO-4 scintillator array. *IEEE Trans. Nucl. Sci.*, 45:681–685, 1998.

[MKA+08] J. C. McGeorge, J. D. Kellie, J. R. M. Annand, J. Ahrens, I. Anthony, A. Clarkson, D. J. Hamilton, P. S. Lumsden, E. F. McNicoll, R. O. Owens, G. Rosner, and A. Thomas. Upgrade of the Glasgow photon tagging spectrometer for Mainz MAMI-C. *Eur. Phys. J. A*, 37(1):129–137, jul 2008.

[Mor09] Markus Moritz. Ansprechverhalten des PROTO 60, Untereinheit des PANDA Detektors, auf hochenergetische Photonen. *Diploma Thesis*, 2009.

[PAN08] PANDA Collaboration. Technical Design Report for PANDA Electromagnetic Calorimeter (EMC), 2008.

[Spa08] S Spataro. Simulation and event reconstruction inside the PandaRoot framework. *Journal of Physics: Conference Series*, 119(3):032035 (10pp), 2008.

[SSH+00] H. Shimizu, Y. Sakamoto, T. Hashimoto, K. Abe, Y. Asano, T. Kinashi, T. Matsumoto, T. Matsumura, H. Okuno, and H. Y. Yoshida. Performance of a PbWO4 crystal calorimeter for 0.2-1.0 GeV electrons. *Nuclear Instruments and Methods in Physics Research Section A: Accelerators, Spectrometers, Detectors and Associated Equipment*, 447(3):467 – 475, 2000.

Erklärung der Urheberschaft

Hiermit versichere ich, dass diese Arbeit ohne Hilfe Dritter und ohne Benutzung anderer als den angegebenen Quellen und Hilfsmittel angefertigt wurde.
Diese Arbeit wurde in gleicher oder ähnlicher Form noch keiner Prüfungsbehörde vorgelegt.

Daniel Andreas Bremer

Gießen, im Februar 2010